creative commons
COMMONS DEED

저작자표시-비영리-동일조건변경허락 2.0 대한민국

이용자는 아래의 조건을 따르는 경우에 한하여 자유롭게

- 이 저작물을 복제, 배포, 전송, 전시, 공연 및 방송할 수 있습니다.
- 이차적 저작물을 작성할 수 있습니다.

다음과 같은 조건을 따라야 합니다:

저작자표시. 귀하는 원저작자를 표시하여야 합니다.

비영리. 귀하는 이 저작물을 영리 목적으로 이용할 수 없습니다.

동일조건변경허락. 귀하가 이 저작물을 개작, 변형 또는 가공했을 경우에는, 이 저작물과 동일한 이용허락조건하에서만 배포할 수 있습니다.

- 귀하는, 이 저작물의 재이용이나 배포의 경우, 이 저작물에 적용된 이용허락조건을 명확하게 나타내어야 합니다.
- 저작권자로부터 별도의 허가를 받으면 이러한 조건들은 적용되지 않습니다.

저작권법에 따른 이용자의 권리는 위의 내용에 의하여 영향을 받지 않습니다.

이것은 이용허락규약(Legal Code)을 이해하기 쉽게 요약한 것입니다.

Disclaimer

dCollection

Ph.D. DISSERTATION

FULL COMPLEX WAVE GENERATION METHODS USING MULTIPLE INTENSITY IMAGES

다중 영상으로부터 완전 광파를 재생하는 방법

Ni Chen

August 2014

DEPARTMENT OF ELECTRICAL ENGINEERING AND
COMPUTER SCIENCE
COLLEGE OF ENGINEERING
SEOUL NATIONAL UNIVERSITY

FULL COMPLEX WAVE GENERATION METHODS USING MULTIPLE INTENSITY IMAGES

다중 영상으로부터 완전 광파를 재생하는 방법

지도 교수 이병호

이 논문을 공학박사 학위논문으로 제출함

2014 년 08 월

서울대학교 대학원

공과대학 전기•정보공학부

Ni Chen

Ni Chen의 박사 학위논문을 인준함

2014 년 08 월

위 원 장 _____ (인)

부위원장 _____ (인)

위 원 _____ (인)

위 원 _____ (인)

위 원 _____ (인)

Abstract

FULL COMPLEX WAVE GENERATION METHODS USING MULTIPLE INTENSITY IMAGES

NI CHEN

DEPARTMENT OF ELECTRICAL ENGINEERING AND

COMPUTER SCIENCE

COLLEGE OF ENGINEERING

SEOUL NATIONAL UNIVERSITY

In the research of optical imaging, both amplitude and phase of light wave are necessary. Since the phase carries important information about a wavefront, we can use it to measure the shape, surface profile and other properties of an object. However, it is difficult to measure the phase by general camera sensors due to its high frequency. Therefore, we need to use special techniques to rebuild both the amplitude and phase of a light

wave. Among these wavefront reconstruction techniques, the widely used one is using intensity measurements but without interferometric approaches.

In this thesis, we develop a fast convergent wavefront retrieval from multiple intensity measurements. Resampling captured diffractive intensity images with different levels makes images that represent different resolutions of an object. Then we can perform separate iterative calculations to the resampled images, therefore reach fast convergence in the reconstruction. Both simulation and experimental results show the convergences of the proposed method is about two times faster than the conventional method in our test images.

In the techniques of hologram generation from multiple view projection (MVP) images, the scientists capture the MVP images under incoherent illumination. My previous works analyzed the parameters that affect the resolution of the reconstructed images, and proposed a lens array shift method to improve the resolution of the reconstructions. Since the lens array shift method introduced movement in the capturing process, in this thesis, I compare the resolution of hologram reconstruction between using rectangular and hexagonal lens arrays to capture the multiple view images. I will show the theory and verify it with simulation

and experimental results.

In the conventional hologram generation from multiple view images, most of the limitations are induced by the lens array used in the multiple view image capturing, which induces the performance limitation. We develop hologram generation from three photographic images captured with only a general camera and without any other optical components. The three images are used to produce orthographic images without sampling limitation introduced by other ingredients. Therefore, we can synthesize high resolution holograms from these orthographic images. The size of the object can be from microscopic to large size objects.

Keywords: Wavefront sensor, Holography, Image processing, Integral imaging, Light field.

Student Number: 2010-31321

Contents

List of Figures

List of Tables

Chapter 1. Introduction

1.1. Role of phase in optical imaging

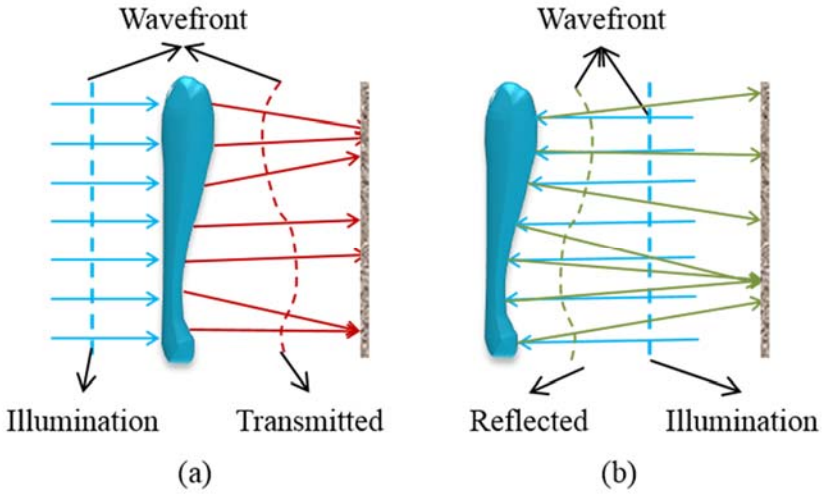

Figure 1.1. How phase contains an object's information: (a) transmittion mode and (b) reflection mode.

A camera sensor cannot directly measure the phase component of an optical field, while it just records the intensity of the optical field. To measure the phase information, we need to know how the phase of an optical field acts. Figure 1.1 shows two normal cases explaining how the intensity distribution reflects the phase of the optical field according to the object which distorts or reflects the optical rays. In Figure 1.1 (a), suppose the object is transparent, it does not change the amplitude of the

light passing through it, but introduces phase delays due to the refractive index. The delays reflect the shape and density of the object, which can be measured. Therefore the material properties of the object, such as pressure, temperature, humidity can be obtained from the measured phase delay [1]. In a reflection mode, as Figure 1.1 (b) shows, the measured intensity carries information about the topology of a reflective object, which can be used for surface profiling [2]. However, the above examples are the ideal cases, in the real world, objects may have absorption, thus make the intensity measurements affected by both the refractive index and the absorption. Therefore, obtaining phase and amplitude of the wavefront needs two or more intensity measurements. These techniques that rebuild phase from intensity measurements are called 'complex-field' imaging techniques or 'full wavefront' imaging technique.

Figure 1.2. A photograph of the bottom of a pool under sunlight.

Figure 1.2 is an example of phase affection we can see in our daily life. It is a photograph of the bottom of a pool under sunlight illumination, and the visible line patterns show the water surface of the pool, which makes the sunlight focusing or defocusing at some areas.

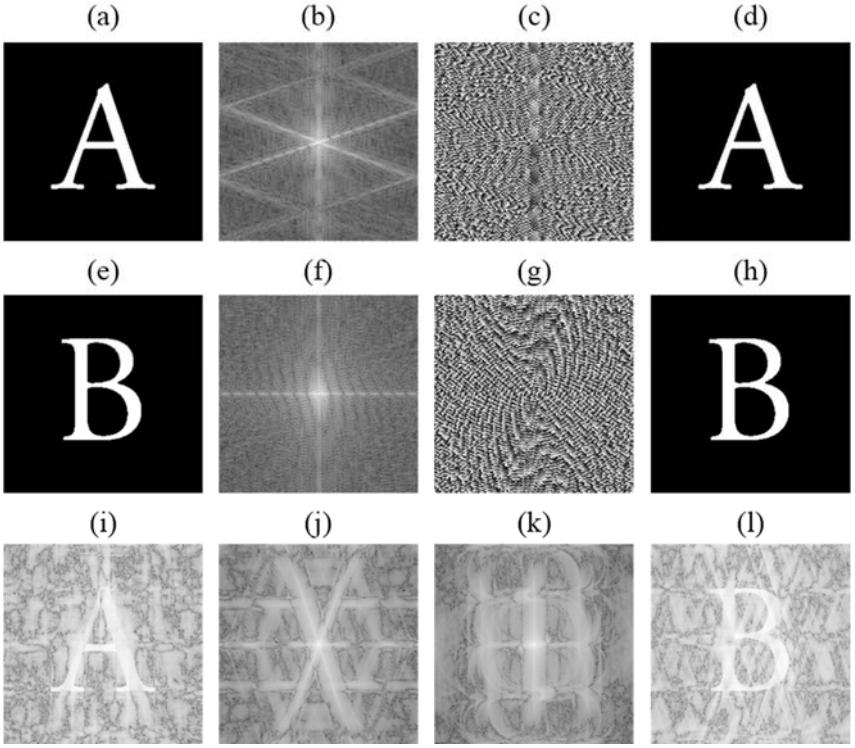

Figure 1.3. Example that shows the importance of phase information in image processing: (a,e) original images; (b, f) amplitude and (c, g) phase of the corresponding Fourier transformed images; reconstructed images (d, h) with both the right amplitude and phase, (i,l) with only phase information, (j, k) with the right phase but wrong amplifute.

Figure 1.3 is an example of the phase affection in image processing.

I performed Fourier transform two character images “A” and “B” (figure 1.3(*a*) and (*e*)), the corresponding amplitude and phase profiles are shown as Figure 1.3(b)(c) and Figure 1.3 (f)(*g*). With both the amplitude and phase, the original images can be reconstructed, as the images of Figure 1.3(d) and Figure 1.3(h) show. Figure 1.3(j) and Figure 1.3(k) are the reconstructions with just the corresponding amplitude information, and Figure 1.3(i) and Figure 1.3(l) are the reconstructions with the amplitude but a wrong phase information. It shows that an image cannot be reconstructed if we use a wrong phase information or without phase information.

There are many techniques for wavefront reconstruction. We can roughly classify them to interferometric or non-interferometric by the light source illumination types. The following sections will introduce the techniques according to the classification.

1.2. Interferometric wavefront reconstruction techniques

The main idea of wavefront reconstruction using interferometric techniques is simple. The object wave $A(x, y)exp[j\varphi(x,y)]$, where $A(x,y)$ is amplitude and $\varphi(x,y)$ is phase, interferers with a known plane reference wave $a(x,y)exp[j\theta(x,y)]$. The measured interferometric intensity pattern

is related to both the amplitude and the phase of the object wave, as Eq.(1.1) describes,

$$\begin{aligned} I(x,y) &= \left|A(x,y)\exp[j\varphi(x,y)] + a(x,y)\exp[j\theta(x,y)]\right|^2 \\ &= |A|^2 + |a(x,y)|^2 + 2|A||a(x,y)|\cos\left[\varphi(x,y) - \theta(x,y)\right]. \end{aligned} \tag{1.1}$$

The object wavefront thus can be reconstructed from this intensity pattern with some special techniques.

1.2.1. Holography

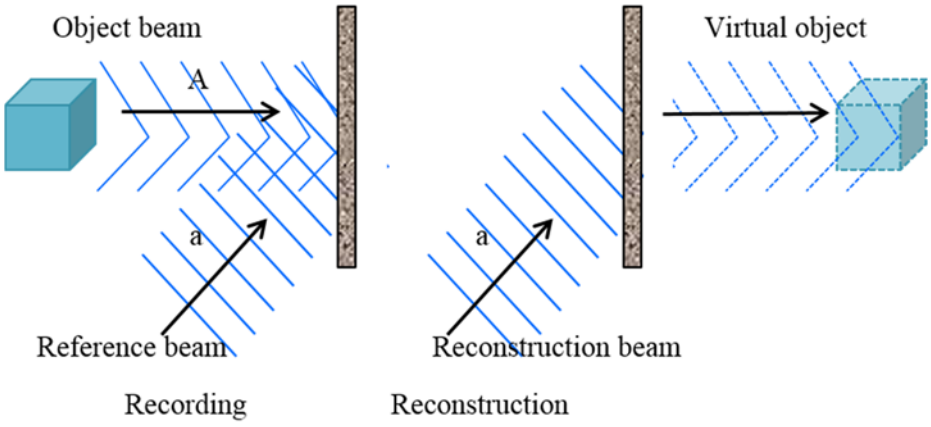

Figure 1.4. Principle of holography: (a) recording, and (b) reconstruction.

As Figure 1.4 (a) and Eq. (1.1) show, the interferometric pattern of an object wave and a reference wave can be recorded. The intensity pattern is a function of both amplitude and phase, which is called “hologram”, means “total recording” [3–5]. In the hologram reconstruction (Figure

1.4 (b)), the reference wave is used to illuminate the hologram, the original wavefront thus can be reconstructed with diffraction from the reconstruction beam. This holography technique was discovered in 1947 by Dennis Gabor [3]. With the development the laser in 1960, the requirement of long coherence length became accessible, allowing sensitive phase measurements [2].

The applications of holography are wide, such as microscopy, high resolution volume imagery, interferometry, imaging through distorting media, holographic data storage, holographic optical elements, security, and holographic display. In this thesis, I focus on the three-dimensional (3D) display of the holography.

1.2.2. Phase-shifting interferometry

As the interference pattern of two waves can be expressed by Eq. (1.1), if the reference wave was changes in phase of σ, it becomes $aexp[j\theta(x,y)]exp[j\sigma(x,y)]$, and the interference pattern becomes

$$\begin{aligned} I(x,y;\sigma) &= |A|^2 + |a(x,y)|^2 \\ &\quad + 2|A||a(x,y)|\cos[\varphi(x,y) - \theta(x,y) - \sigma]. \end{aligned} \tag{1.2}$$

If the shift step of the phase is $\pi/2$, and four intensity patterns $I(x,y;0)$, $I(x,y;\pi/2)$, $I(x,y;\pi)$, and $I(x,y;3\pi/2)$ are reordered, the phase of the object can be calculated by [6]

$$\varphi'(x,y) = \tan^{-1}\left\{\frac{I(x,y;\pi/2) - I(x,y;3\pi/2)}{I(x,y;0) - I(x,y;\pi)}\right\}, \tag{1.3}$$

and the amplitude of the object can be calculated by

$$A'(x,y) = \frac{1}{4}\frac{I(x,y;0) - I(x,y;\pi)}{\cos\left[\varphi(x,y) - \theta(x,y)\right]}. \tag{1.4}$$

Since the intensity measurement is related to the cosine of the phase, phase unwrapping is required. Four intensity patterns can also be captured with single-shot to simplify the capturing complexities [7,8].

Obviously, holography is an ideal 3D display because the constructed wave front is identical to that of the original scene. The first hologram that recorded 3D objects was made in 1962 by Yuri Denisyuk [9] , Emmett Leith and Juris Upatnieks [5]. The image changes as the position and orientation of the viewing system change in the way as if the object were still present, thus making the hologram appears three-dimensional. However, the long coherence length and powerof the optical source requirement and obtaining high quality recording material are still issues. Recently, the computer generated hologram (CGH) and the digital holography (DH) became polular because of their advantages in fast capturing and their versatility in processing.

1.3. Non-interferometric wavefront reconstruction

techniques

It is necessary to remove the complexity and the coherent limitations in the interferometric techniques. This can be achieved by using partially coherent illumination [10]. Or we can use a set of intensity images measured with a known complex transfer function to calculate the phase. This takes the advantage of the modern computerization, thus leads a versatile and simple experimental imaging system. The fllowing sections give a brief introduction.

1.3.1. Shack-Hartmann sensors

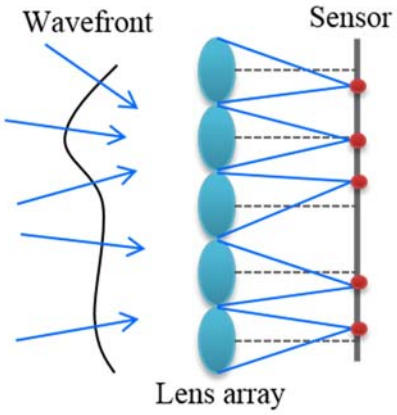

Figure 1.5. Scheme of Shack-Hartmann sensors.

In the techniques of Shack-Hartmann sensors, it places a lenslet array in front of a camera. The locations of the focal spots reflect the directions of the incoming lights, which is re-interpreted as wavefront slope [11].

In case the sensor pixel size of the camera is much smaller than the lenslet, the phase retrieval can be accurate and robust to noise. Since each lenslet measures only one lateral phase, this technique has the low resolution problem. Therefore this technique is popular in wavefront sensing for adaptive correction of atmospheric turbulence, where incoming light is not coherent and resolution is not critical.

1.3.2. Iterative techniques

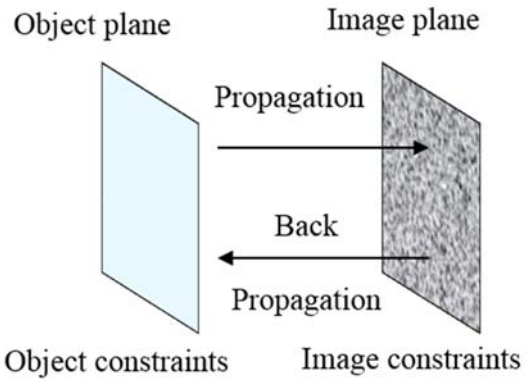

Figure 1.6. Scheme of iterative technique.

Almost all the iterative phase retrieval techniques are based on the Gerchberg-Saxton (GS) method [12]. In the GS method, bounces between in-focus and Fourier domain images are performed, as Figure 1.6 shows. At each step, an estimate of the complex-field is updated with measured or a priori information of the object [13–15]. Fresnel transformed images can be used instead of Fourier images [16, 17]. In

this case, the accuracy of the phase retrieval is affected by defocus between the images [18], and the optimal amount of defocus is object-dependent. Large propagation distances produce better diffraction contrast, thus makes these techniques work better with larger propagation distances [18, 19]. Phase solutions with this techniques are not unique, but are likely to be correct [20], and many techniques exist for lessening the solution error [21]. In imaging, using more than two intensity images [22, 23] or phase masks [24] can reduce the solution error.

Due to the fact the optimal transfer function is object-dependent and the simplicity of this technique, the 'iterative technique' remains a popular technique for wavefront reconstructions.

1.3.3. Direct methods

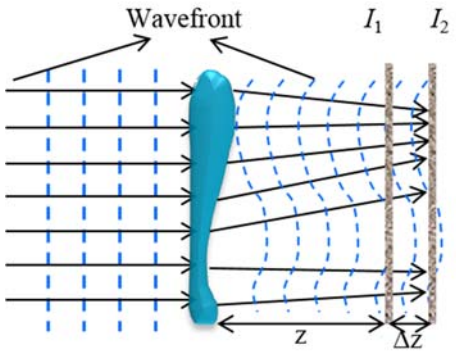

Figure 1.7. A phase object changes the wavefront of a plane wave which travels through the object.

Figure 1.7 shows the action when a plane wave travels through a phase object. The wavefront after passing through the object is bent and the directions of the light rays are changed according to the thickness and the refractive index of the object. The phase delay is associated with the transversed distribution of intensity which is given by the transport of intensity equation (TIE) [25–27]:

$$\frac{\partial I(x,y)}{\partial z} = -\frac{\lambda}{2\pi}\left(\nabla_{\perp} \cdot I(x,y)\nabla_{\perp}\varphi(x,y)\right), \tag{1.5}$$

where $I(x, y)$ is the intensity measurement along the optical axis, λ is the illumination wavelength [28] and $\nabla_{\perp}$ denotes the lateral gradient operator and φ is the phase distribution of the wavefront at a distance of z from the object surface. The TIE can break through the diffraction limitation of the imaging system [29], which is due to its ability of complex-field reconstruction under partially coherent light illumination [30]. It also does not need phase unwrapping [31]. The limitations in the TIE technique include: Wavefront is noise-sensitive which comes from the low phase contrast requirement; optical system is spectrum dependent because defocus is related to the object spatial frequency; exact depth difference measurement is difficulty; precise motion of camera or object in sequence intensity images capturing can not be well controlled.

1.4. Hologram generation with incoherent illumination

Holography provides useful methods for dealing with 3D information of objects. Since it first came out, the scientists developed various applications based on 3D nature of the hologram. Those applications capture interference patterns of 3D objects using coherent optical imaging, and manipulate them to the expected results. However, since recording the hologram requires coherent optics, the imaging system is bulky and hard to handle. In addition, because of the coherent illumination, it is hard to get hologram of the distant objects or background scene. The scientists have developed methods under incoherent illumination to remove the necessity of the coherent in the hologram capturing. Old techniques of recording holograms under incoherent illumination were interferometry of light waves scattered from the same object point. An object is of many points, therefore, if a spatially incoherent or quasi-monochromatic light illuminates this object, each point is self-spatially coherent and thus can create an interference pattern with the light coming from the mirrored image of the point [32–37]. There are also some rather new techniques which record hologram under incoherent illumination, I simply describe these techniques in the following sections. Because of these reasons, we can’t simply classfy

holography to just interferometric or non-interferometric technique, hence, I put it in the following section.

1.4.1. Scanning holography

Scanning holography is a widely used technique that works under incoherent illumination [38–40]. Under spatially incoherent illumination, a Fresnel zone plate scans a 3D scene, and we integrate the light intensity at each scanning position by a point detector, which makes a Fresnel hologram. However, the scanning induces heavy time consumption and complicated laser alignments. Although we can solve these problems by Fresnel zone-plate coded hologram [41], the imaging in the optical regime should still be done.

1.4.2. Fresnel incoherent correlation holography

Fresnel incoherent correlation holography (FINCH) is a motionless technique for getting digital Fresnel hologram [42–45]. In this technique, it uses a digital camera to record the object wavefront which passes through a spatial light modulator (SLM). The SLM acts as a beam-splitter, makes each spherical beam of each object point splitting into two spherical beams with different curvatures. Summation of the entire interferences amoung all the couples of spherical beams creates the

Fresnel hologram of the 3D object. It can avoid the twin-image problem [46] by recording three different holograms each with a difference phase on the SLM and superposing them in a final Fresnel hologram. Due to the multiple holograms recording, dynamic hologram recording is not convenient. In addition, the SLM used to display the diffractive optical element (DOE), may cause low signal-to-noise ratio in the hologram reconstruction when the 3D scene is intricate [47].

1.4.3. Hologram generation from multiple view images

Hologram generation from multiple viewpoint projection images is an efficient way to synthesize hologram without coherent illumination without an extreme stable optical system or wave interference. First, it picks up the two-dimensional projections of a 3D scene, and then digitally process synthesize the hologram. The synthesized hologram is equivalent to a conventional digital hologram. We can also get the MVP images by shifting a camera mechanically, and capturing one single view image at a time [48–52]. We also can get the MVP images using a camera array [53], or a lens array [54–58]. After the MVP images' capturing, we can calculate one/two-dimensional [48–50, 52, 54, 57, 59–62] holograms, Fourier holograms [48, 51, 52, 59], Fresnel holograms [51, 52, 58, 61, 63], and protected correlation holograms [61, 64]. However, these

previous methods can be applied to only Fourier or Fresnel hologram, require indirect synthesis, or produce not exact but adjusted holograms. J.-H. park *et al*. proposed a method for creating both of Fourier and Fresnel holograms from multiple view images by using orthographic projection geometry [59].

1.5. Outline of this thesis

As the previous sections introduced, there are various kinds of optical imaging. In this thesis, all the contents are about optical imaging with multiple images. One topic is the wavefront reconstruction from diffracted intensity images, which are along the optical axis; the other one is the holographic imaging, while the hologram is synthesized from MVP images that captured under incoherent illumination.

Chapter 2 describes a fast convergent computer algorithm for improving the calculation time and the quality of the reconstructed images in wavefront reconstruction from multiple intensity measurements. The coherent illumination requires well configured environment, and has disadvantages, such as speckle and limited object size. Thus optical imaging techniques under incoherent or partially coherent illumination came out. The technique of incoherent hologram

synthesis is a popular one.

Chapter 3 proposes a resolution comparison analysis of hologram reconstruction in Fourier hologram generation from orthographic projection images using a lens array. It turns out that the resolution of the hologram reconstructions is limited, and the previous improvement method induced movement in the capturing process.

The difficulty of significant improvement in the hologram generation from orthographic images based on internal imaging comes from the introduced lens array in the capture process. Thus, removing the lens array in the capturing is urgent. Chapter 4 describes a hologram generation method from orthographic images which are extracted from two photos captured by a general camera under sunlight illumination.

Finally, Chapter 5 states conclusions and my future work.

Chapter 2. Fast wavefront reconstruction algorithm from multiple diffracted intensity images

2.1. Wavefront reconstruction from diffracted images

A major advantage of wavefront reconstruction based on a series of diffracted intensity images using only single beam illumination is the simplicity of setup. Here I propose a fast convergent algorithm for wavefront calculation using single beam illumination: the captured intensity images are resampled to a series of intensity images, ranging from the highest resampled image to the lowest resampled image; each image has half the number of pixels as the previous resampled image. Phase calculation at a lower resolution is used as the initial solution phase in a higher resolution. This corresponds to separately calculating the phase for the lower and higher frequency components. Iterations on the low frequency components do not need to be performed on the higher frequency components, thus making the convergence of the phase retrieval faster than the conventional method. The principle is verified by both simulation and optical experiments.

Optical wavefronts which are reflected by or transmitted through an

object have amplitude and phase modulation by the object. If light field is passing through an object, the measured wavefronts carry information related to the phase delay of the object which is due to the refractive index and shape of the object. Thus when the measured wavefront is known, the thickness and shape of an object can be obtained. If a light field is reflected by an object, the measured wavefront carry information regarding the topology of the object and, thus can be used to measure the surface profile of the object. Hence wavefront measurements can be utilized in many areas, including imaging, surface profiling, adaptive optics, astronomy, ophthalmology, microscopy and atomic physics. However it is not possible to detect the phase using general detectors because the oscillation frequency of light is too high to permit being followed by detectors. Therefore, many attempts to acquire phase information have been made in the past. The techniques for this can mainly be categorized into two types, one being based on interferometry and the other being a phase retrieval method based on capturing the intensity of the object beam. The interferometry method, generally referred to as holography, records the interference pattern of an object beam and a reference beam. This process converts phase information to intensity modulation [3]. However, introducing a reference beam

requires a complicated interference experimental setup, which also induces some other problems in hologram reconstruction, such as the DC term problem and the twin image problem. These problems require a more complicated experiment setup [65, 66].

Wavefront reconstruction using phase retrieval techniques does not require any reference beam. Generally, several diffracted intensity images and some post digital image processing are needed. Deterministic phase retrieval using the transport of intensity equation (TIE) works on the condition of paraxial approximation, which limits its application in general cases [30, 67, 68]. The iterative phase retrieval methods mainly involve the use of the Gerchberg-Saxton (GS) algorithm and Yang-Gu (YG) algorithm, which use prior knowledge of the object as constraints [12, 14, 69]. For the case of an object with an unknown constraint, it is difficult to reconstruct the wavefront using the GS and YG algorithms. Various approaches have been proposed to solve this problem. One type of approach is to obtain the object indirectly – using an aperture to capture small images and then obtain the object constraint [70] or using a known illumination pattern as a constraint instead of the object constraint [71]. The other type of approach is to use two or more intensity images with variations – which can be produced by capturing intensity

images with different focuses [72], translating an aperture transversely [73] or shifting the illumination [74]. However, all of these approaches require additional optical components and involve complicated post digital processes.

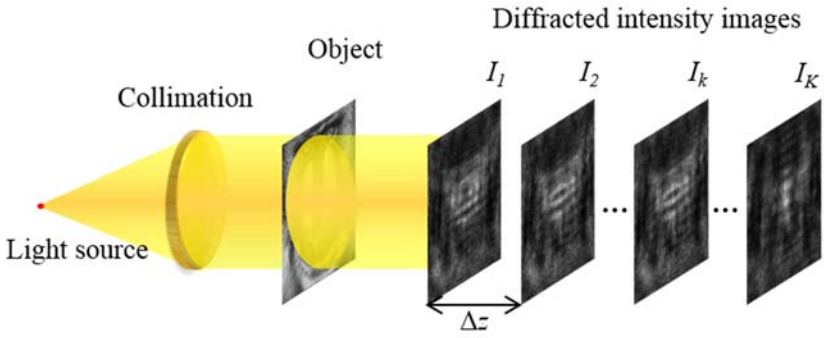

Figure 2.1. Capturing process of the speckle intensity images for SBMR.

Pedrini *et al*. used images captured at axially translated planes, i.e., single-beam multiple-intensity reconstruction (SBMR) [75]. The SBMR method has the simplest capturing setup compared to the other phase retrieval methods that are based on multiple intensity images [72–74]. It uses only a camera. It has also been applied in some other research areas, such as measuring the shape, deformation and angular displacement of 3D objects [76, 77]. Phase retrieval using multiple intensity images captured at a series of planes can detect spatial frequencies at different sensitivities. Therefore, the significant amount of the data carried by

these intensity images makes this approach very robust and rather stable to the effects of noise [78]. Figure 2.1 shows the experimental scheme for capturing intensity images by the SBMR method. The object is illuminated by a collimated light source. The charge-coupled device (CCD) is shifted along the optic axis and captures the diffracted intensity images with an interval Δz between two adjacent images. The total number of intensity images is K.

It is known that the number of the captured images affects reconstruction quality, i.e., more intensity images result in higher quality reconstructions [79]. However, capturing more intensity images requires more movement steps of the camera or the object, which makes the captured images sensitive to small misalignments in the experimental setup, thus the noise induced to the captured intensity images becomes more serious. Furthermore, more captured intensity images require more experimental time, which makes the method not capable for use in dynamic object or real-time applications. In order to improve the capabilities of SBMR [75], beam splitters [80], spatial light modulator (SLM) [81, 82], deformable mirror (DM)[83] were used to achieve single-shot or single-plane intensity image capturing processes. However, beam splitters cause the attenuation of illumination light. In

the case of SLM and DM, the simplicity of the experimental setup is sacrificed. A random amplitude mask [84] and random phase plate [85] have also been used to transform low frequency components to fast varying high frequencies, which requires less iterations for reconstruction. However, an amplitude mask results in the diminution of light energy and the use of a phase plate requires difficult fabrication.

(a) (b)

Figure 2.2. Example of resampling an image (b) with 128 sampling points and (a) with 64 sampling points.

Multi-scale signal representation is a very efficient tool that can be used in signal and image processing [86, 87]. It represents signals or images with different resolutions – the highly scaled images carry the high spatial frequencies of an image, and the low scaled images carry the low spatial frequencies of the image. This is reflected by one example, as shown in Figure 2.2. Figure 2.2 (b) contains the low frequencies of the

image [88]. In the conventional phase retrieval method, because the high frequency components of the object vary faster than the low frequency components, the variation between two diffracted intensity images is larger for the higher frequency components of the object than the low frequency components of the object. Therefore, less iterations are needed to recover the high frequency than the low frequency components. This is why the convergence of the iterations proceeds rapidly in the beginning, and then becomes very slow. In this study, we optimized the SBMR method by using a multi-scale technique. The captured diffractive intensity images are resampled to several resolution images. Phase retrieval is first performed on the images resampled with a lower resolution and then transferred to images that are resampled with a higher resolution. This corresponds to performing more iterations for the low frequency components than the high frequency components. Suppose one captured image is resampled to A number of level images, and the number of iterations on each level is B. Then, for the low frequency components on the smallest resolution image, the number of iterations would be AB, and for the high frequency components on the highest resolution image, the number iterations would be just B. Moreover, because the image that is resampled with a low resolution contains less

pixels, the time required for one iteration on this image is less than that for an image resampled with a higher resolution. Because the image resampling process corresponds to separating the high frequency components from the low frequency components, when iterations on the low frequency components are done, it is not necessary to do this on the high frequency components. Therefore, although I do more iterations on the images resampled with low resolutions than on images resampled with high resolutions, the total time consumption for the iterations is not increased by as much as in the conventional method. Furthermore the large variation between intensity images results in a fast convergence rate in the iteration process [67], and the variation between images that are resampled with low resolution is increased. For these reasons, the proposed algorithm achieves a faster convergence than the conventional method. I describe the principle of the proposed method in section 2.2, and the results of computer simulations and experiments to verify the proposed method are shown in sections 2.3 and 2.4.

2.2. Principle

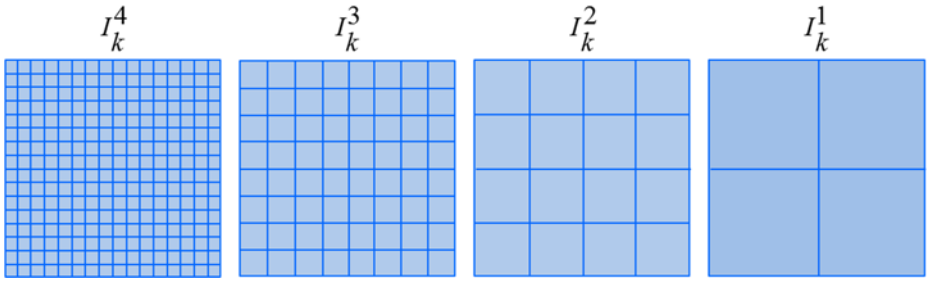

Figure 2.3. Example of resampling process for the image with M=4.

In my proposed algorithm, the capturing process is the same as the conventional method, as shown in Figure 2.1. A series of diffractive intensity images, I_k, are captured along the optical axis at different positions, where k is an integer from 1 to K. When the captured images have a lateral resolution of 2^M pixels, the captured intensity image can be resampled into M different level images. Therefore, the resampled image of the m^{th} level has 2^m sampling points, where m is an integer from 1 to M. The resampling process starts from the captured image which has the most sampling points, i.e., where $I_k^m = I_k^M$. The next sampling level I_k^{m-1} can be expressed as

$$I_k^{m-1} = Z\left\{I_k^m, 2^{m-1}\right\}, \tag{2.1}$$

where Z is the bicubic interpolation, in which the value of the pixel that needs to be calculated is determined by the average value of its 16

weighted neighbor pixels. The weight of each neighbor pixel is calculated using 16 equations which are given by the gradients in both the horizontal and vertical directions, and the cross derivatives at each of the four corners of the pixel square [89]. The second parameter of the Z operation is the image size after performing an interpolation. This process is performed until the resampling level reaches the first resampling level I_k^1. The whole resampling process of I_k is performed for all of the captured intensity images $I_1 \ldots I_K$. After this resampling process, we have a total of $M \times K$ number of intensity images, and these images are grouped by resampling level. For example, the m^{th} group of the resampled intensity images is $G_m = \{I_1^m, I_2^m, \ldots, I_K^m\}$. The bicubic interpolation was used to preserve the fine detail with better performance than the other common interpolation algorithms such as bilinear interpolation and nearest-neighbor interpolation [89]. The sinc interpolation may be thought to be the most appropriate method for band-limited optical fields, but oscillations at the signal borders may restrict image processing. Particularly in small sized images, noticeable ripples from the image borders may occupy a substantial part of the image [90–92]. Consider the reduced size of the resampled images in our approach, i.e., 2^1 to 2^N pixels; sinc interpolation is not appropriate in my method.

Figure 2.3 shows an example of the resampling scheme for an image that has 2^4 pixels.

Figure 2.4 shows the flowchart of my proposed algorithm. The numbers with a circle in this figure are the step notations of the procedure. In the flowchart, N is the number of iterations, and f is a binary value of 1 or -1. Here 1 denotes forward propagation and -1 denotes backward propagation. The conventional iteration method is performed from the first resampling level, i.e., M=1 and G_1= $\{I_1^1, I_2^1 \ldots I_K^1\}$. The solution at this level is interpolated to the next resampling level (M=2) and used as the initial solution for the next resampling level. This process is continued until the highest resampling level G_M is reached. It should be noted that this is different from optical ptychography, which simply uses a part of the intensity images and extends the image areas until the full intensity images are addressed [93]. The details of the iterative procedure are as follows:

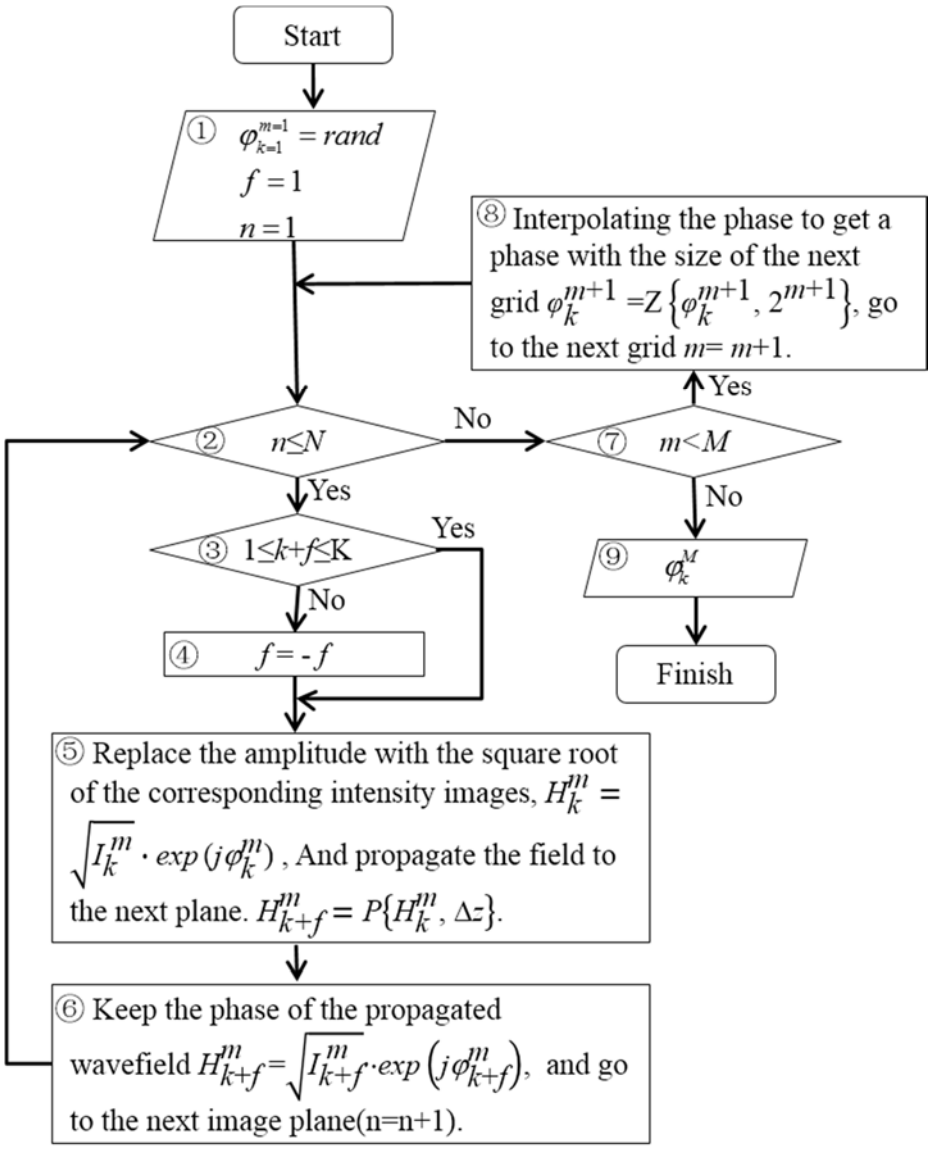

Figure 2.4. Flow chart of the proposed algorithm.

Step 1: Setting the initial value. The procedure starts from the first image at the first level, i. e., k=1 and m=1. The initial complex field is a composite of an amplitude and a random initial phase. The square root

of the intensity I_1^1 is used as the amplitude, and the initial phase is a random distribution that has 2^1 pixels, which is the size of the lowest sampled level.

Step 2: Checking the current iteration number. When the iteration number reaches the maximum iteration value, go to the next level, i. e., go to step 7; otherwise, do an iteration on the current level, i.e., go to step 3.

Step 3: Decide which process should be continued according to whether the current image is the last, the first image or not in the current group. If not, do the propagation to the next image, i. e., go to step 5; otherwise, do the inverse propagation, i.e., go to step 4.

Step 4: Making the propagation direction inversely.

Step 5: Building the complex wave field, use the square root of the current intensity distribution as the amplitude and the previous calculated phase as the phase: $H_k^m = (I_k^m)^{1/2} \cdot \exp(j\varphi_k^m)$. Then propagating this wavefield to the next plane: $H_{k+f}^m = P\{H_k^m, \Delta z\}$. Here, P means the angular spectrum propagation of the Rayleigh-Sommerfeld diffraction [94].

$$\begin{aligned} & P\{O(x,y),z\} \\ & = \Im^{-1}\left(\Im[O(x,y)] \times \exp\left[-j\frac{2\pi z}{\lambda}\sqrt{1-\lambda^2u^2-\lambda^2v^2}\right]\right), \end{aligned} \tag{2.2}$$

where $\Im$ is the operation of the Fourier transform, λ is the illumination wavelength, and (u, v) are the coordinates after propagation.

Step 6: Updating the amplitude of the calculated complex wavefront H_{k+f}^{m} in the next plane by using the square root of the intensity image at this plane: $H_{k+f}^{m}=(I_{k+f}^{m})^{1/2}\cdot\exp(j\varphi_{k+f}^{m})$. Also update the index of the iteration and intensity image. Shift the process to the next image plane, i.e., go to step 2.

Step 7: If the current level is the last level, retain the calculated phase in step 6 as the final solution. Otherwise, using the solution in step 6 as the initial phase of the next level, go to step 8.

Step 8: Interpolate the calculated phase in step 6 to a size of the next level using Eq. (2.1). Here the second parameter in this equation should be 2^{m+1}. Do step 2 to step 8 until the iteration number that is set previously is reached.

From the final calculated wave field, the wavefront at all the captured image planes can be obtained by propagating this field, and the object can be reconstructed by back propagating the wavefront to any image plane.

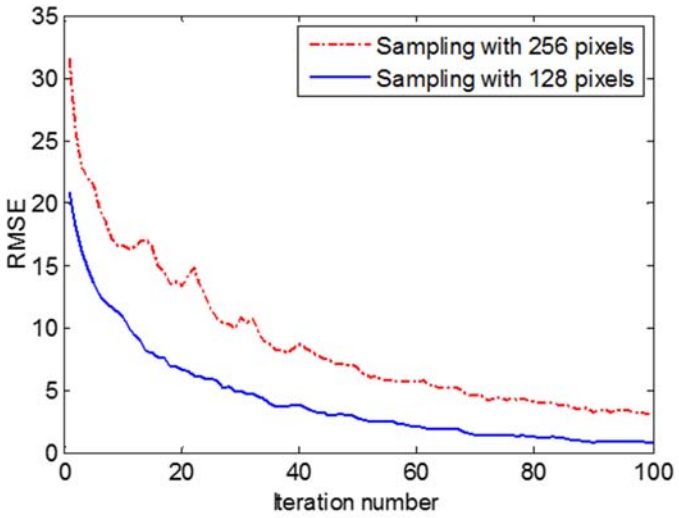

Figure 2.5. Iterative convergence for images with different sampling points.

As presented in the introduction, the images sampled with less points carry the low frequency components of the image, which requires less iterations in the phase reconstruction, and vice versa. This is indicated in figure 2.5. The two images with 128 and 64 pixels in figure 2.2(a) and figure 2.2(b) are reconstructed using the conventional error reduction method. The normalized root mean square errors (RMSEs) according to the iteration number are plotted. The red dashed and blue solid lines indicate the convergence of the iterations for figure 2.2(a) and figure 2.2(b), respectively. It can be seen that the iterative convergence for the image sampled with 64 pixels is faster than that which has 128

sampling points.

Resampling the images also produce increased variations between images. Figure 2.6 shows an example of the variations between diffracted images along the optical axis with variant resampling levels. Figure 2.2 is used to generate two diffracted images with a slice depth difference. The two images are resampled to 8 number of levels respectively. The variations for different level images are then calculated. The horizontal axis represents the level number and the vertical axis represents the variations with the corresponding sampling level on the horizontal axis. This figure demonstrates that the variation between images at two planes along the optical axis increases with decreasing sampling numbers, which is the requirement for achieving fast convergence in the iterative phase retrieval techniques. This can be attributed to the fast convergence of phase retrieval because the amount of defocus between the diffracted intensity images affects the accuracy of the phase retrieval [67]. The amount of defocus can be obtained with a larger depth difference, in this method, by just carrying out a post-resampling of the diffracted images.

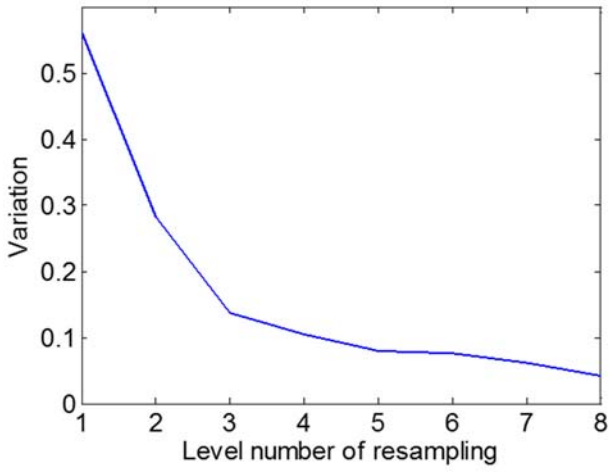

Figure 2.6. Pixel variation along the axis at each resampling level number.

Based on the two points presented above, we can speculate that by resampling diffracted intensity images with different levels, it is possible to perform a faster convergence iterative phase retrieval.

2.3. Simulations

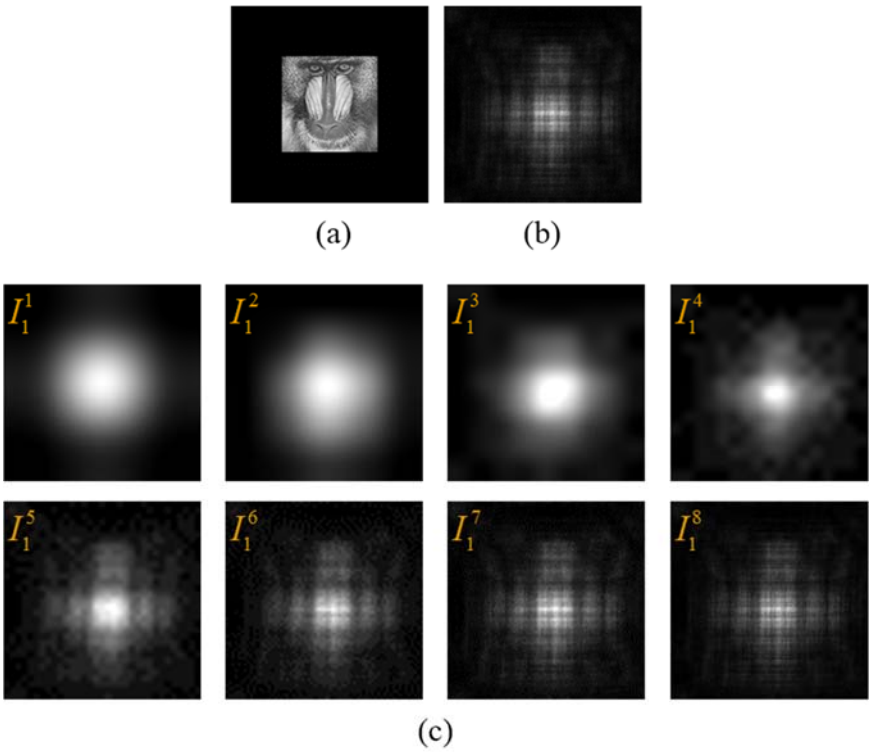

Figure 2.7. Example of the resampling one intensity image: (a) Amplitude image of the object used in the numerical simulations, (b) the first captured intensity image and (c) the resampled images.

In the simulation, the object is a composite of the amplitude pattern shown in Figure 2.7(a) and a random phase distribution which ranges from 0 to 2π. The size of the object is 256×256 pixels. The object is padded with zeroes in order to avoid energy leaking out of the edges of the captured intensity images. In the experiment, this corresponds to making almost all the intensity distribution within the camera sensor area.

The object is illuminated by a light source with a wavelength of 532 nm. Five intensity images are captured by a CCD camera which has pixel pitch of 4.65μm. The nearest capture plane is located away from the object plane with a distance of z=30 mm, and the interval between two adjacent capture planes is Δz=5 mm. Figure 2.7(b) is the calculated diffracted intensity image at the first plane and Figure 2.7(c) shows the 8 resampled images of the first image I_1.

The original image is reconstructed by the conventional and the proposed methods, respectively. The normalized root mean square error(RMSE) is used to measure the results. The RMSE is defined as:

$$RMSE = \frac{\sqrt{\sum_{m,n}\left(\left|I(m,n)\right| - \left|I'(m,n)\right| \right)^2}}{\sqrt{\sum_{m,n}\left|I(m,n)\right|^2}} \times 100\%, \qquad (2.3)$$

where I_1 and I_2 are the original image and proposed reconstructed image. Figure 2.8 shows the RMSE with respect to time consumption. The proposed and conventional reconstructions are plotted as a red dashed line and a blue solid line, respectively. Figure 2.8(b) is the square area crossed by the blue dashed line in Figure 2.8(a). From Figure 2.8(b) it can be seen that the conventional method reached a minimum RMSE value at about 4.5 seconds, while the proposed method arrived at the

same RMSE value in about 2.2 seconds, which is about 51.11% faster than the conventional method.

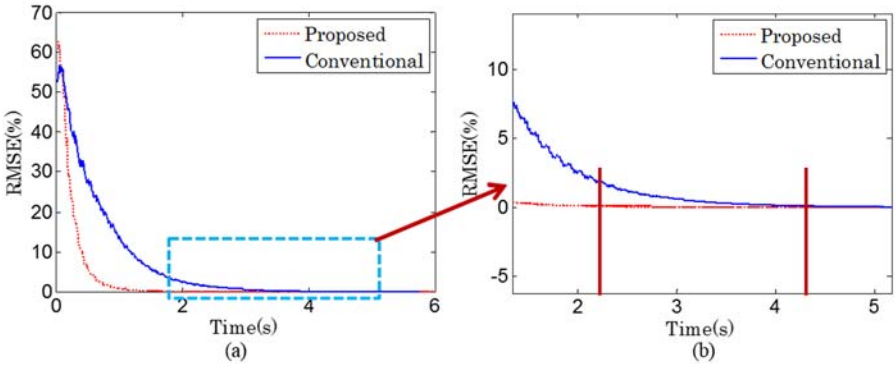

Figure 2.8. RMSE with respect to the time consumption. Part (b) is the magnification of the square area crossed by blue dashed lines in part (a).

2.4. Experimental results

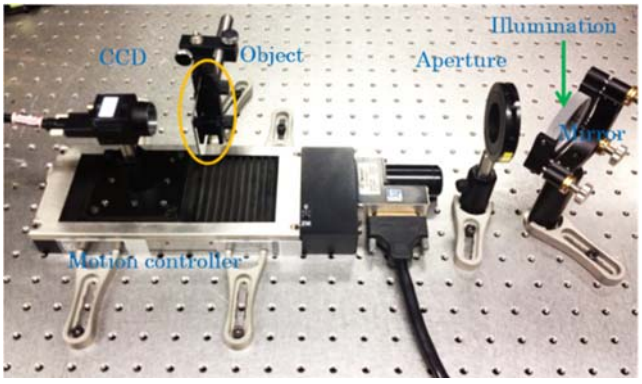

Figure 2.9. Experimental setup.

In the experiment, a laser with a wavelength of 532nm is used to illuminate a Newport USAF 1951 resolution chart. In the resolution chart,

the background area is opaque while the lines area is transparent. The light wave after the object is modulated in the lines area and stopped in the opaque area. Thus the optical wavefront just after the object reflects the shape of the resolution chart. By reconstructing the wavefront at the object location, the shape image of the object can be reconstructed. Seven diffracted intensity images were captured by Point Grey FL2-14S3M/C CCD camera. The first image was located at 40mm from the target and the interval between two images is 8mm. Figure 2.9 shows the experimental setup.

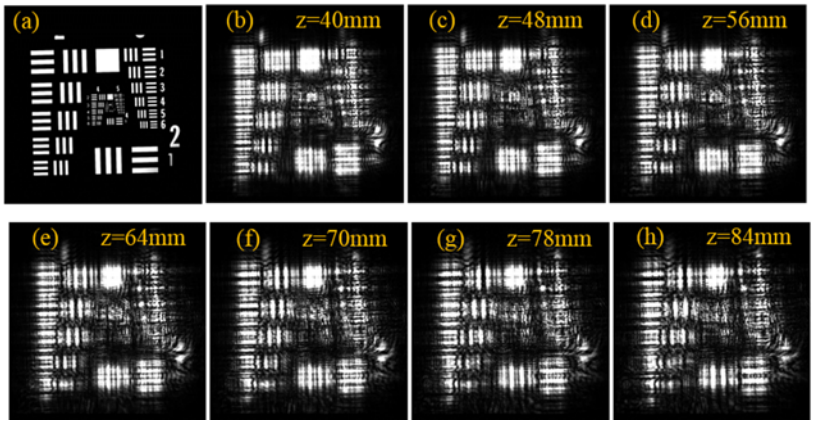

Figure 2.10. Captured images: (a) the directly captured image of the object; (b)-(h) the captured diffracted intensity images.

Figure 2.10(a) shows the directly captured image of the resolution chart and Figure 2.10(b)-(h) show the captured diffracted intensity images. The wavefront at the first plane was calculated by the

conventional and the proposed methods. The object was reconstructed by digitally propagating the calculated wavefront.

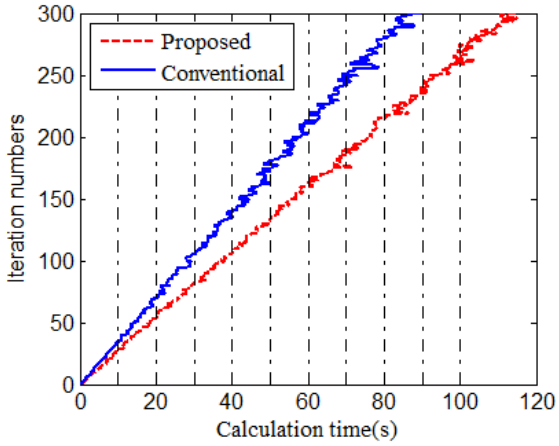

Figure 2.11. Time consumption versus the number of iterations.

Three hundred iterations were performed in both the conventional and proposed methods. The corresponding time consumption is shown in Figure 2.11. The horizontal dashed lines are the chosen timelines for convergence comparison. The red dashed line and blue solid line represent the proposed and conventional methods, respectively. The horizontal axis values of the two intersection points on each horizontal dashed line indicate the numbers of iterations used in the conventional and proposed methods, respectively, and are listed in Table 2.1.

Table 2.1. Iteration number requirement for the crossed points in Figure 2.11.

Time(s) / Iterations	10	20	30	40	50	60	70	80
Conventional	35	75	106	141	173	203	243	280
Proposed	27	30	82	105	133	159	186	215

The corresponding reconstructed images for the iteration numbers in Table 2.1 are shown in Figure 2.12. The lines crossing the "2" character are plotted in Figure 2.13(b). Figure 2.13(a) shows a plot corresponding to the direct captured object, i.e., Figure 2.10(a), which is used as the ground truth. From Figure 2.13, it can be seen that, in the conventional method, about 80 seconds was needed to obtain the best reconstruction. In order to find how much time is needed for the proposed method to reconstruct the image with a quality similar to this image, we compared this image with the proposed reconstructed images for time consumptions of 10s, 20s, 30s, 40s, 50s, 60s, 70s, and 80s. The correlation coefficients are plotted as Figure 2.14. From this figure, a similar image was obtained with the proposed method within 40 seconds. This means that the proposed method is capable of obtaining a similar reconstruction to the original with a time consumption of about 40 seconds, which is about two times faster than the conventional method.

This result is also in agreement with the simulated results. The small stagnation in the reconstructions by the proposed method is induced by the noise in the experimental images.

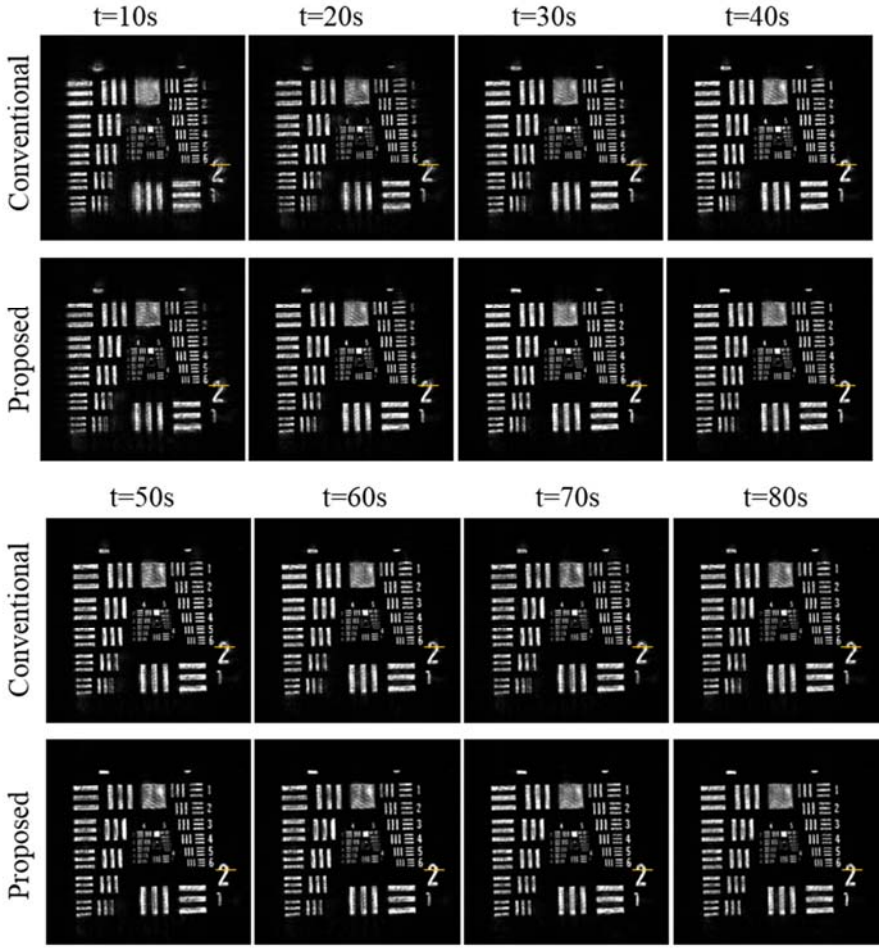

Figure 2.12. The conventional and proposed reconstructions at the timelines.

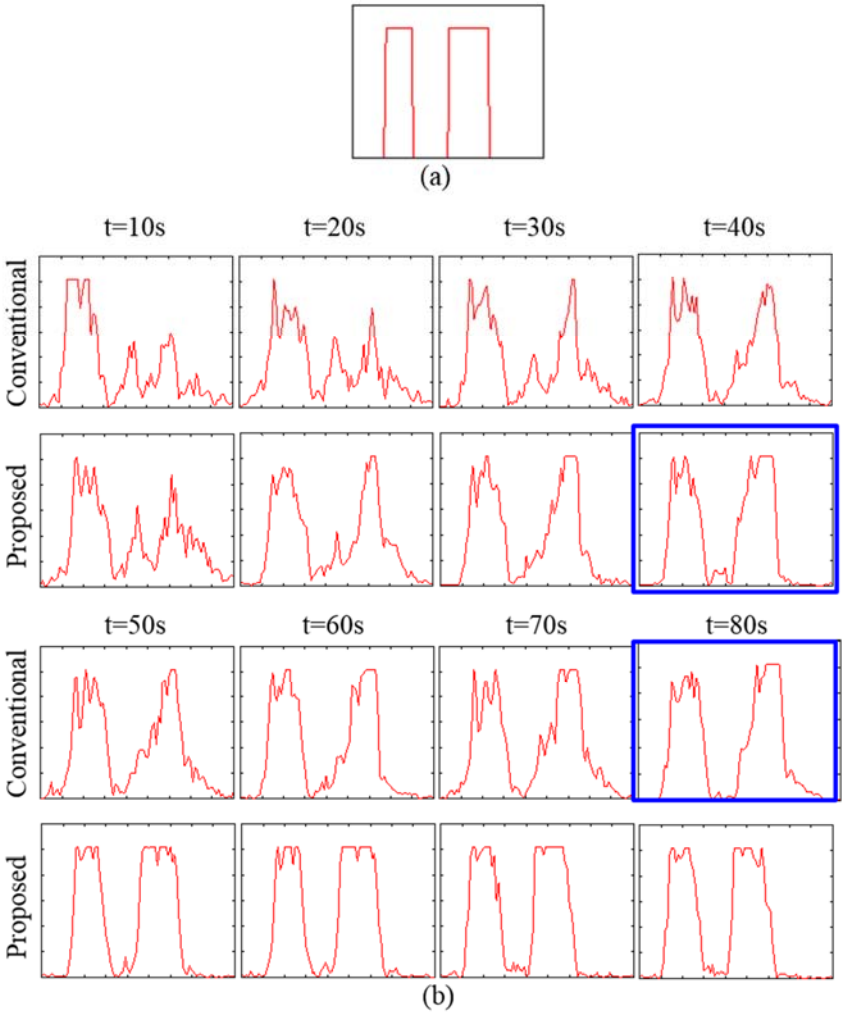

Figure 2.13. The plotted images along the lines (a) on the directly captured image of Figure 2.10(a) and (b) on the reconstructed images of Figure 2.12.

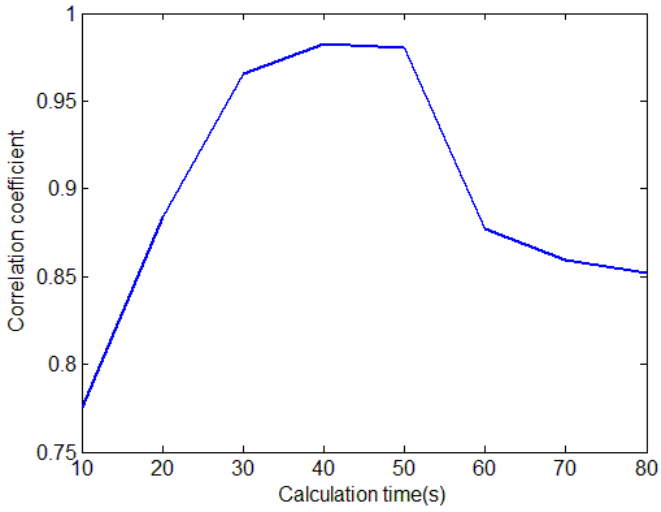

Figure 2.14. The correlation coefficients between each reconstructed image by the proposed method and the conventional image reconstructed with a time consumption of 40 seconds.

2.5. Chapter summary

I propose a fast convergence wavefront reconstruction algorithm by resampling diffractive intensity images. Both simulation and experimental results show that the convergence of the proposed method is about two times faster than the conventional method for the case of my test images. We expect that the proposed method can be applied to real-time phase retrieval application with further development of computer processing unit speed.

Chapter 3. Resolution improvement on hologram generation using lens array

3.1. Introduction of hologram generation from orthographic images

Holography provides useful methods for dealing with 3D information of objects. Since it has been first proposed, various applications have been developed based on 3D nature of the holography. Those applications capture hologram of 3D objects using coherent optical system, and manipulate it to get desired results. However, since the capturing process of the hologram needs laser and coherent optics, the overall system is bulky and hard to handle. Also due to the difficulties in the illumination, it is hard to get hologram of the distant objects or background scene.

Hologram generation from multiple viewpoint projection (MVP) images is an efficient way to synthesize hologram without coherent illumination and an extreme stable optical system or wave interference at all. The two-dimensional projections of a 3D scene are acquired first, and then digitally processed to synthesize the hologram. The synthesized hologram is equivalent to a conventional digital hologram. The MVP images can be obtained by shifting a camera mechanically, and capturing

one single view image at a time [48–52]; or can be captured using a camera array [53] or can be captured with a single shot through a lens array [54–58]. After the capturing process, one or two dimensional [49, 50, 52, 54, 59–61] holograms, Fourier holograms [48, 51, 52, 59], Fresnel holograms[51, 52, 58, 61, 63], and protected correlation holograms [61, 64] can be calculated. However, these previous methods can be applied only to Fourier or Fresnel hologram, require indirect synthesis, or produce not exact but modified holograms. J.-H. Park *et al*. proposed a method for generating both of Fourier and Fresnel holograms from multiple view images by using orthographic projection geometry [59]. This method has advantages including exact Fourier hologram calculation and manipulation of the reconstructions' locations. But the resolution limitation in the hologram reconstruction is a problem, which comes from not enough light field sampling by the lens array. The parameters analysis of the hologram reconstruction was been shown and a lens array shift method was proposed to enhance the resolution of the reconstructed images. However, they induced mechanical motion problem [95]. In this chapter, I propose a method to improve the hologram reconstructs' resolution by using hexagonal lens array. Section 3.1 introduces the Fourier hologram generation from orthographic

images. In section 3.3, I show the theory and the experimental results using hexagonal lens array.

3.1.1. Fourier hologram generation from orthographic view images

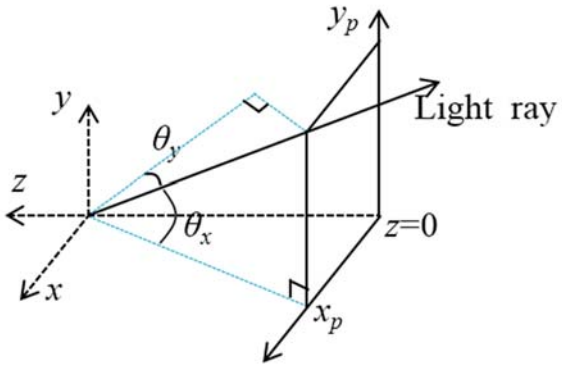

Figure 3.1. Definition of orthographic images

Orthographic projection view images of a 3D object is defined as Figure 3.1, each point on one projection image $P(x_p, y_p; z)$ has the same projection angle (θ_x, θ_y). This is unlike usual perspective projection geometry where all the projection lines are converged to a vanishing point. The orthographic geometry has the projection lines all parallel to each other. The projection image coordinates can be written as

$$\begin{aligned} x_p &= x + z\tan\theta_x, \\ y_p &= y + z\tan\theta_y. \end{aligned} \tag{3.1}$$

3.1.2. Orthographic projection images obtained by a lens array

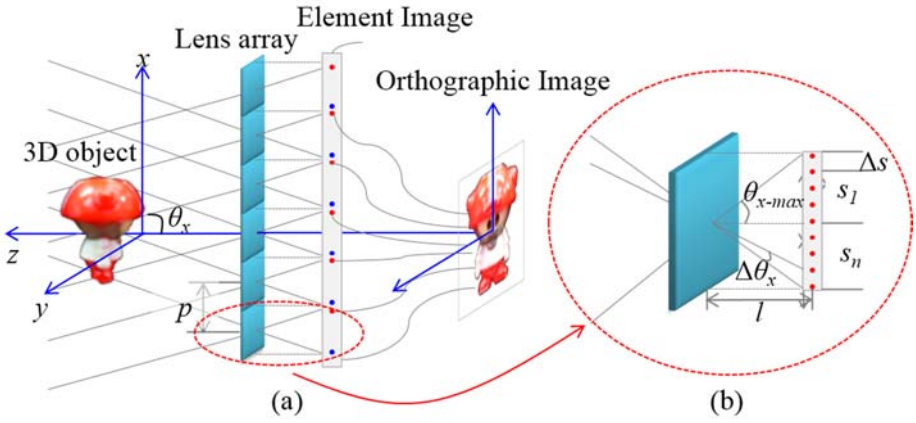

Figure 3.2. Orthographic projection images generation using a lens array[96].

Table 3.1. Parameter definition in the capturing process.

Parameters	Description
l	Focal length of the lens array
p	Lens pitch of the used lens array
Δs, Δt	Pixel pitch of the elemental images
s, t	Local position of pixels in each elemental image
$\Delta\theta_x$, $\Delta\theta_y$	Projection angle interval of the pixels in the elemental images
$\theta_{x\text{-}max}$, $\theta_{y\text{-}max}$	Maximum projection angle

It is a heavy work to capture large amount of orthographic projection images. Due to the efficiency of lens array used in integral imaging, the orthographic view images can be obtained by imaging the 3D objects

through a lens array with some post imaging processings [96, 97]. As Figure 3.2 shows, when the 3D object is imaged through a lens array, each elemental lens of the lens array forms one of the images of the 3D object at its focal plane, which is called elemental image. The parameters in this figure are depicted in Figure 3.2(b) and defined in Table 3.1. If the pixels are collected from each elemental image at the same local position (s, t), they form an orthographic projection image of the object with the projection angle of

$$\begin{aligned} \tan\theta_x &= \frac{s}{l}, \\ \tan\theta_y &= \frac{t}{l}. \end{aligned} \tag{3.2}$$

Because the micro lens and the sensor pixels are always square, $\Delta\theta=\Delta\theta_x=\Delta\theta_y$, $\theta_{max}=\theta_{x\text{-}max}=\theta_{y\text{-}max}$, and $\Delta s=\Delta t$. If the lens array consists of $N_x\times N_y$ elemental lenses and each elemental image consists of $M_x\times M_y$ pixels, the generated orthographic image will have $N_x\times N_y$ pixels and the total number of the generated orthographic images will be $M_x\times M_y$. Therefore, from the elemental images captured by a single shot using a lens array, a lot of orthographic projection images can be generated.

3.1.3. Fourier hologram generation using orthographic projection images

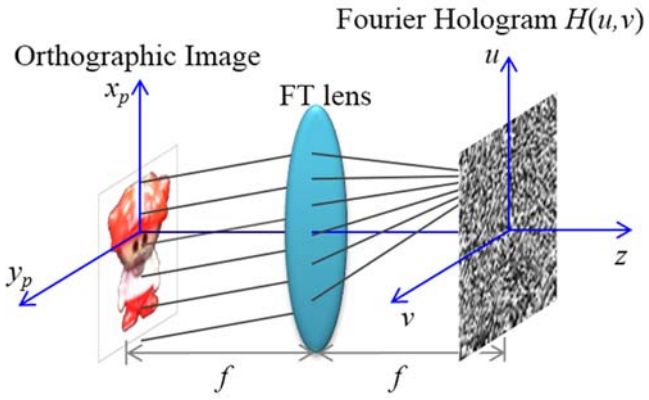

Figure 3.3. Fourier hologram generation from the orthographic projection images.

The Fourier transform can be performed by using a thin lens. The lens makes a plane wave into a point in the lens focal plane [88], and the position of the point depends on the propagation direction of the wave. Therefore, the Fourier hologram of a 3D object can be obtained by integrating each of the orthographic images, which corresponds to each point on the hologram, whose proof is shown below [98, 99].

As $P_{s,t}(x_p, y_p)$ denotes the orthographic projection image of the projection angle corresponding to s and t, as shown in Figure 3.2(b), $P_{s,t}(x_p, y_p)$ is related to the object function $O(x, y, z)$ by

$$P_{s,t}(x_p, y_p) = O\left(x_p - \frac{zs}{l}, y_p - \frac{zt}{l}; z\right). \quad (3.3)$$

Using orthographic images $P_{s,t}(x_p, y_p)$, the Fourier hologram can be generated by

$$H(s,t) = \iint P_{st}(x_p, y_p) \exp\left[-j\frac{4\pi}{\lambda l}\left(x_p s + y_p t\right)\right] dx_p dy_p, \quad (3.4)$$

where λ is the wavelength of illumination light source. Replacing (s, t) with continuous variables (u=Ms, v=Mt), the following equation can be obtained:

$$H(u,v) = \iint P_{u/M,v/M}(x_p, y_p) \exp\left[-j\frac{4\pi}{\lambda l M}\left(x_p u + y_p v\right)\right] dx_p dy_p, \quad (3.5)$$

where M is the magnification factor. If M is set to -2f/l and b is set to $2/\lambda l$, by substituting $P_{u/M,v/M}(x_p, y_p)$ in Eq.(3.5) with Eq. (3.3), it can be easily verified that Eq. (3.5) is the Fourier hologram of the object $O(x, y, z)$

$$H(u,v) = \iiint O\left(x, y; z\right) \times \exp\left[-j\frac{\pi}{\lambda f}\left(\frac{z}{f}u^2 + \frac{z}{f}v^2 - 2xu - 2yv\right)\right] dxdydz, \quad (3.6)$$

where f is the focal length of the Fourier transform lens [100]. Therefore the proposed method given by Eq. (3.4) produces Fourier hologram of the 3D objects.

3.1.4. Limitations in the reconstructions

Figure 3.4 shows an example of the reconstructed plane images for two plane images “C” and “B” located at different planes along the object axis [59]. Figure 3.4(a) and Figure 3.4(b) show the computational and optical reconstructions, respectively. It can be noted that even with simple object, the resolution of the reconstructed images is low. This limitation has also been demonstrated in [98].

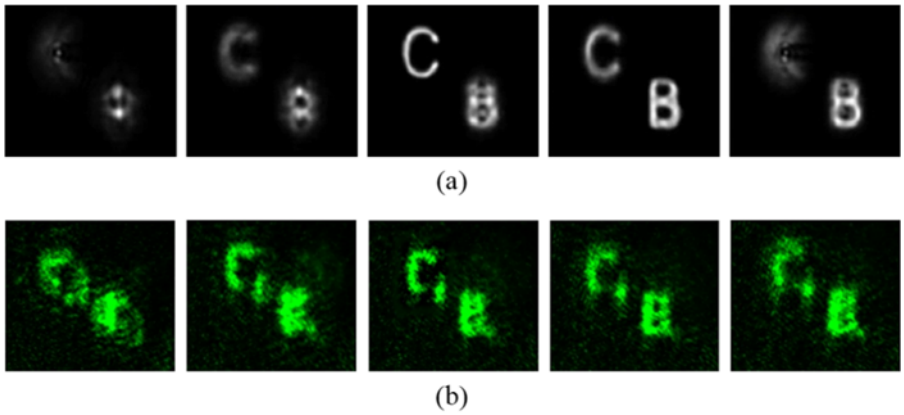

Figure 3.4. One example of (a) computationally and (b) optically reconstructed images.

3.2. Resolution enhancement of the hologram reconstruction by using hexagonal lens array

There are many researches for improving the resolution of the reconstructed images in integral imaging or holograms generated based on integral imaging, such as time multiplexing method [101–103], synchronously moving micro-optics method [103, 104], micro lens array

scanning method [105], and lens array shift method [95, 106]. These non-stationary lens array methods have demonstrated efficient resolution enhancement of integral imaging [107, 108]. However, they induced mechanical motion problem. All these methods are based on the strengthened sampling of spatial-angular light ray distribution using non-stationary lens array. For the lens array, most of those methods use rectangular lens array and therefore the light ray distribution is captured in a rectangular grid. However, hexagonal grid provides higher packing density and gives a more accurate approximation of circular regions compared with the rectangular grid. In addition, the sampling points of the hexagonal grid are uniformly connected in the sense that each sampling point is located at a fixed distance to all the six adjacent pixels. Hence, hexagonal grids have been used in a wide variety of research fields [109, 110]. It has been known that circularly band limited signals are sampled more efficiently by hexagonal grids than by rectangular grids [111–113]. It has also been reported to enhance the display resolution using the hexagonal sampling strategy [114, 115].

In this section, we compare the resolution of the hologram reconstruction based on integral imaging with a rectangular lens array and a hexagonal lens array. A hexagonal lens array and a rectangular lens

array are used in the elemental image capturing, and holograms are generated from the captured information following the method presented in Ref. [59]. Using hexagonal lens array corresponds to the hexagonal sampling of the 3D object and thus can accommodate more in bandwidth. Although there have been usages of hexagonal lens array in integral imaging, there has been no study on its usage for hologram generation based on integral imaging. Also, although Mishina *et al*. [63] reported an analysis on the aliasing in the hologram generated using integral imaging, their hologram generation method is different from the method considered in this thesis and hence their analysis cannot be applied in my work. To my best knowledge, this is the first report that provides the quantitative analysis and experimental verification on the resolution enhancement of the hologram synthesis using hexagonal lens array. In Section 3.5.2, I analyze the resolution enhancement quantitatively. In Sections 3.5.3 and 3.5.4, simulation and experimental results are presented to verify the analysis.

3.2.1. Theory

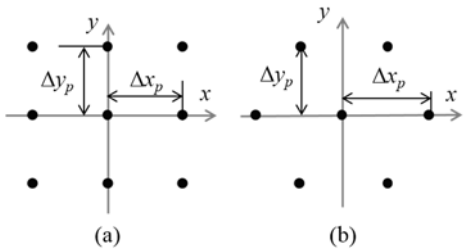

Figure 3.5. Sampling in spatial domain. (a) Rectangular sampling grid. (b) Hexagonal sampling grid.

Figure 3.5 shows the rectangular sampling and hexagonal sampling. The sampling intervals Δx and Δy are defined as the distances between two adjacent columns and two adjacent rows, respectively. For an object field of o(x, y), the rectangular sampled object field õ$_{rec}$(x, y) and hexagonal sampled object field õ$_{hex}$(x, y) can be described by Eqs. (3.7) and (3.8), respectively:

$$\tilde{O}_{rec}(x,y) = \sum_{m,n} O(x,y)\delta(x - m\Delta x)\delta(y - n\Delta y), \tag{3.7}$$

$$\tilde{O}_{hex}(x,y) = \sum_{m,n} O(x,y)\delta\left(x - (2m+n)\Delta x\right)\delta(y - n\Delta y). \tag{3.8}$$

In the Fourier hologram generation based on integral imaging, we define the lens pitch of the lens array as the distance between the centers of two adjacent lenses, as Figure 3.6 shows. Suppose a rectangular lens array and a hexagonal lens array have the same lens pitch p. Using these

two lens arrays, integral Fourier holograms are generated with the method described in section 3.2. Note that in the integral Fourier hologram method the orthographic image is generated by extracting one pixel per each elemental image. Hence the object field is first sampled with the lens array in the orthographic image generation step and this affects the final hologram resolution.

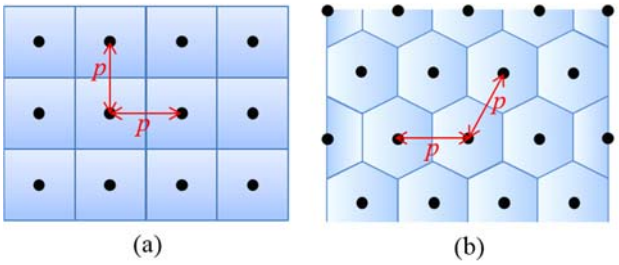

Figure 3.6. Sampling with lens array. (a) Sampling by rectangular lens array. (b) Sampling by hexagonal lens array.

The original object is sampled with rectangular or hexagonal lens array, as shown in Eqs. (3.7) and (3.8). The sampling interval is $\Delta x=\Delta y=p$ in the rectangular sampling and $\Delta x= p/2$ and $\Delta y=\sqrt{3}/2p$ in the hexagonal sampling. I analyzed the lateral size and the spatial frequency bandwidth of the reconstruction using these two types of lens arrays.

Suppose the original object has a limited size $2L_x \times 2L_y$. As the reconstruction is the inverse Fourier transform of the hologram and the

hologram is discretized with Δu and Δv, by the sampling theory, the reconstruction is a repetition of the original object field. The repetition period is given by $\lambda f/\Delta u=\lambda f/M\Delta s=\lambda f/2f\Delta\theta_x=\lambda/(2\Delta\theta_x)$ along the horizontal direction and $\lambda f/\Delta v=\lambda f/M\Delta t=\lambda f/2\mathrm{f}\Delta\theta_y=\lambda/(2\Delta\theta_y)$ along the vertical direction [4], as Figure 3.7 shows. In order to avoid overlapping in the reconstruction, the object size should be smaller than this repetition period. Thus the maximum size of the object that can be reconstructed without overlapping can be described as

$$2L_{x'}=\frac{\lambda}{2\Delta\theta_x},\ 2L_{y'}=\frac{\lambda}{2\Delta\theta_y}. \tag{3.9}$$

Because the projection angle intervals $\Delta\theta_x=\Delta s/l$ and $\Delta\theta_y=\Delta t/l$ are only related to the pixel pitch of the capturing sensor, the maximum sizes of the reconstructed object are the same for the rectangular lens array case and hexagonal lens array case when the image sensors are the same.

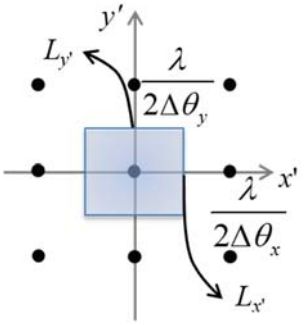

Figure 3.7. Spatial domain representation of the reconstruction.

The spatial frequency bandwidth of the reconstruction is determined by two factors, i.e., sampling of the object field with the lens array grid in the orthographic image generation step and the limited lateral size of the synthesized Fourier hologram. The sampling of the object field makes the reconstruction spectrum be replicas of the spatial frequency spectrum of the original object field. The limited lateral size of the synthesized Fourier hologram defines cut-off spatial frequency in this spectrum.

Let us first consider the effect of the sampling in the orthographic image generation. The spectrum of the sampled object field is given by

$$\begin{aligned} & FT\left[\tilde{O}_{rec}(x,y)\right] \\ & = FT[o(x,y)] \otimes \sum_{m,n} \delta\left(f_x - \frac{m}{p}\right)\delta\left(f_y - \frac{n}{p}\right), \end{aligned} \tag{3.10}$$

$$\begin{aligned} & FT\left[\tilde{O}_{hex}(x,y)\right] \\ & = FT[o(x,y)] \otimes \sum_{m,n} \delta\left(f_x - \frac{2m+n}{p}\right)\delta\left(f_y - \frac{n}{\sqrt{3}p}\right), \end{aligned} \tag{3.11}$$

for rectangular lens array and hexagonal lens array, respectively and $\otimes$ represents convolution. Equations (3.10) and (3.11) show that the spectrum of the object field is repeated with different grid as depicted in Figure 3.8. Therefore the maximum radial spatial frequency that can be

reconstructed without aliasing is given by

$$f_{\rho,rec} = \sqrt{f_x^2 + f_y^2} \le \frac{1}{2p},$$
$$f_{\rho,hex} = \sqrt{f_x^2 + f_y^2} \le \frac{1}{\sqrt{3}p}, \tag{3.12}$$

for rectangular lens array and hexagonal lens array case, respectively. The maximum spatial frequency is $f_{\rho,rec}=1/2p$ and $f_{\rho,hex}=1/\sqrt{3}p$. Hence, the resolution enhancement of a ratio $f_{\rho,hex}/f_{\rho,rec}=2/\sqrt{3}$ can be expected in hexagonal lens array case in comparison with the rectangular lens array case.

The limited lateral size of the Fourier hologram defines the cut-off spatial frequency of the reconstruction. The horizontal and vertical sizes $2L_u$ and $2L_v$ of the synthesized Fourier hologram $O(u, v)$ are determined by the maximum projection angle in the orthographic image generation. From the geometry of the lens array, the synthesized Fourier hologram in the rectangular lens case has a rectangular shape of the lateral size $2L_v=2L_u=4f\theta_{x,max}=2fp/l$. On the contrary, it has a hexagonal shape of the lateral size $2L_u=4f\theta_{x,max}=2fp/l$ and $2L_v=4f\theta_{y,max}=4fp/(\sqrt{3}l)$ in hexagonal lens case. The cut-off spatial frequency area is then given by the same shape as that of the generated hologram with their horizontal size $2f_{x,max}=2f_{y,max}=2p/l\lambda$ in rectangular lens array case, and the horizontal size

$2f_{x,max}=2L_u/\lambda f=2p/l\lambda$ and vertical size $2f_{y,max}=2L_v/\lambda f=4p/\sqrt{3}l\lambda$ in hexagonal lens array case as shown in green lines in Figure 3.8. Then in the case of no aliasing (due to sufficiently small elemental lens pitch p), the maximum spatial frequency range that can be reconstructed is slightly larger in the case of rectangular lens array. However, in case of aliasing as shown in Figure 3.8, the hexagonal shape spatial frequency range reduces the amount of the aliasing with the same elemental lens pitch p and the object bandwidth, presenting better image quality than the rectangular lens array.

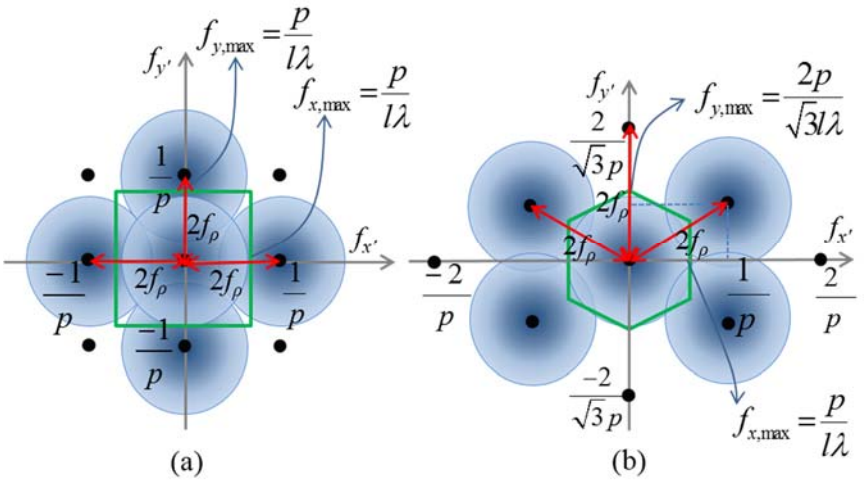

Figure 3.8. Spatial frequency domain representation of the hologram.
(a) Using rectangular lens array. (b) Using hexagonal lens array.

3.2.2. Preprocess for the hexagonal element images

With hexagonal lens array, the shape of each element image is hexagonal.

We use a rectangular mask that contains one element image in its exterior to preprocess the hexagonal element images to rectangular element images, as shown in the left image of Figure 3.9(a). The pixel value of the area that covers the element image is set to '1', or else, the values are set to '0'. By multiplying the mask and each rectangle that just covers one element image pixel by pixel, each element image can be separated. With this separated element images, the sub images can be generated, as Figure 3.9(b) shows.

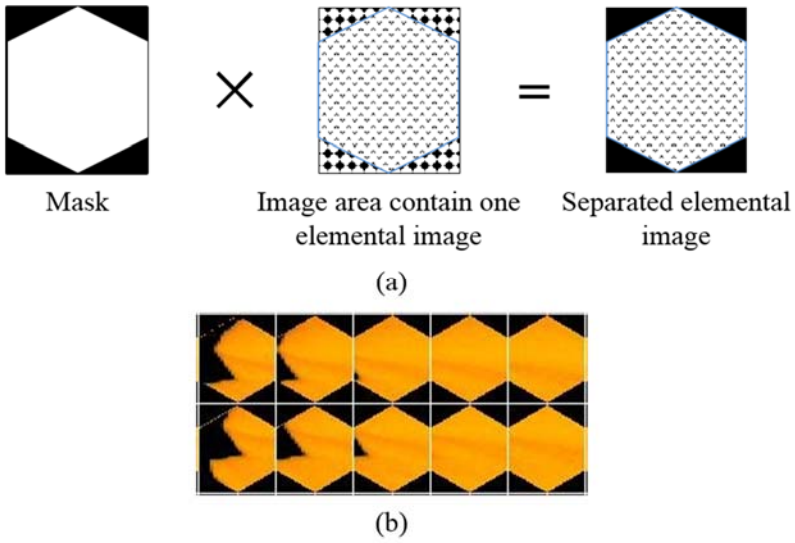

Figure 3.9. Preprocess of the captured elemental image using hexagonal lens array: (a) Extract single elemental image from the captured element image, and (b) part of elemental images after the above process (a).

3.2.3. Orthographic projection image generation using hexagonal elemental images

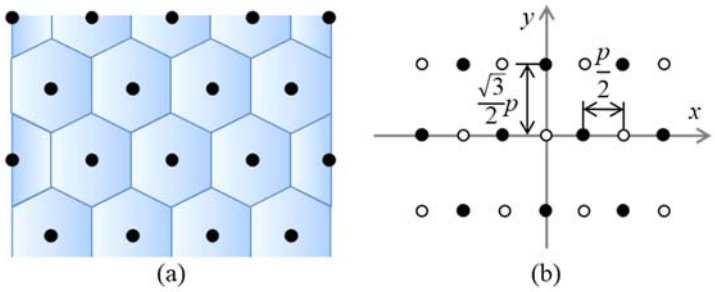

Figure 3.10. Zero padding method. (a) Pixel distribution in an orthographic image. (b) Zero padding of an orthographic image.

In the case of using hexagonal lens array, one orthographic image is a collection of the pixels in each elemental image with the same local position [59, 116, 117], the pixel distribution of one orthographic image can be represented by Figure 3.10(a), in which the hexagons mean the elemental image areas. The sampling points of the object, which correspond to the pixel distribution of the orthographic images, are aligned as the filled circles in Figure 3.10 (b). The sampling intervals of the object are $p/2$ along horizontal direction and $\sqrt{3}/2p$ along vertical direction. Here the sampling intervals mean horizontal or vertical distance between neighboring horizontal or vertical lines connecting filled circles. In my implementation, one zero value point is padded as

represented by open circles in Figure 3.10(b) between two filled circles along the horizontal direction. The Fourier hologram is then generated from the orthographic images using the method in Ref. [59].

3.2.4. Simulations

Figure 3.11. Plane object used in the simulation.

Two simulations were performed: one is using rectangular lens array as a reference, and the other is using hexagonal lens array. In the simulations, one plane image was used as the object, as Figure 3.11 shows. The distance from the plane image to the lens array is 50 mm. The lens pitch is 1 mm. Figure 3.12 shows the elemental images. The size of the elemental images is 4000(H)×5000(V) pixels, and the pixel count of each elemental image is 50(H)×50(V) pixels for rectangular lens array and 50(H)×58(V) pixels for the hexagonal lens array.

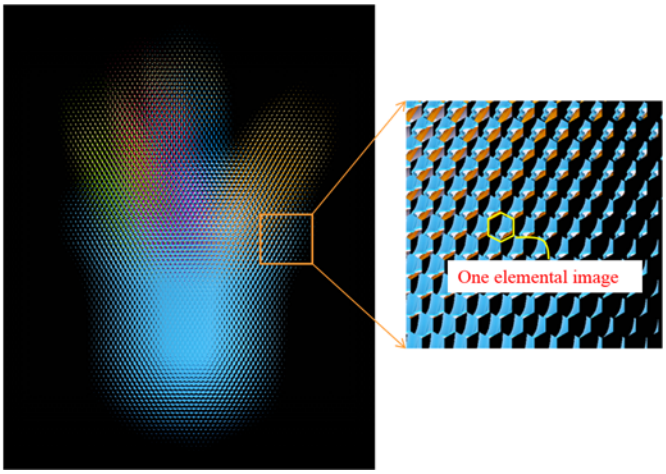

Figure 3.12. Elemental image generated with hexagonal lens array.

With the zero padding method described in previous section, orthographic images are generated as Figure 3.13 shows.

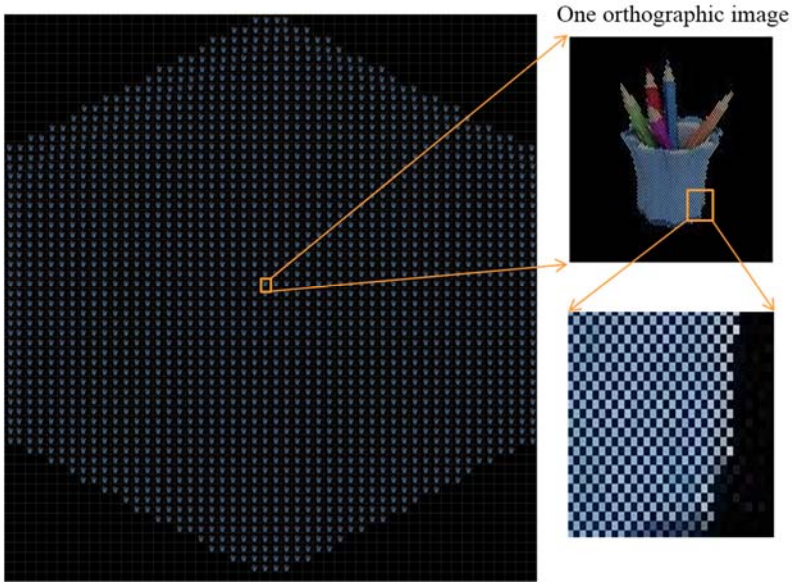

Figure 3.13. Orthographic image generated from the elemental images captured with hexagonal lens array.

From the generated orthographic images, holograms of red, green and blue components are generated separately. Figure 3.14 shows the amplitude and phase of the holograms generated from the red component. Note that in Figures 3.14(a) and 3.14 (c), the contrast was adjusted for better visibility. The red, blue and green images are reconstructed from the three holograms and then synthesized together to get the color reconstruction.

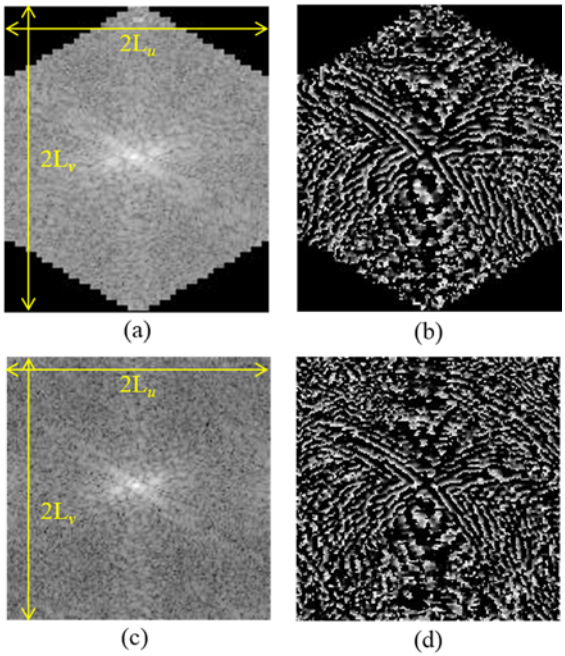

Figure 3.14. Generated hologram for red component. (a) Amplitude and (b) phase profile of the generated hologram using hexagonal lens array. (c) Amplitude and (d) phase profile of the generated hologram using rectangular lens array.

Table 3.2. Key parameters for the two lens arrays.

	No. of EI	p	Δy_p	$\Delta s=\Delta t$	$\Delta\theta_x=\Delta\theta_y$	$\theta_{x,max}$	$\theta_{y,max}$
Rectangle	100×80	1mm	1mm	20μm	0.382°	9.55°	9.55°
Hexagon	116×80	1mm	0.87mm	20μm	0.382°	9.55°	11.03°

Table 3.3. PSNR and NCC values of the reconstructed images.

	Rectangular lens array	**Hexagonal lens array**	**Improvement**
PSNR	21.83dB	24.25dB	2.42dB
NCC	0.9649	0.9758	0.0109

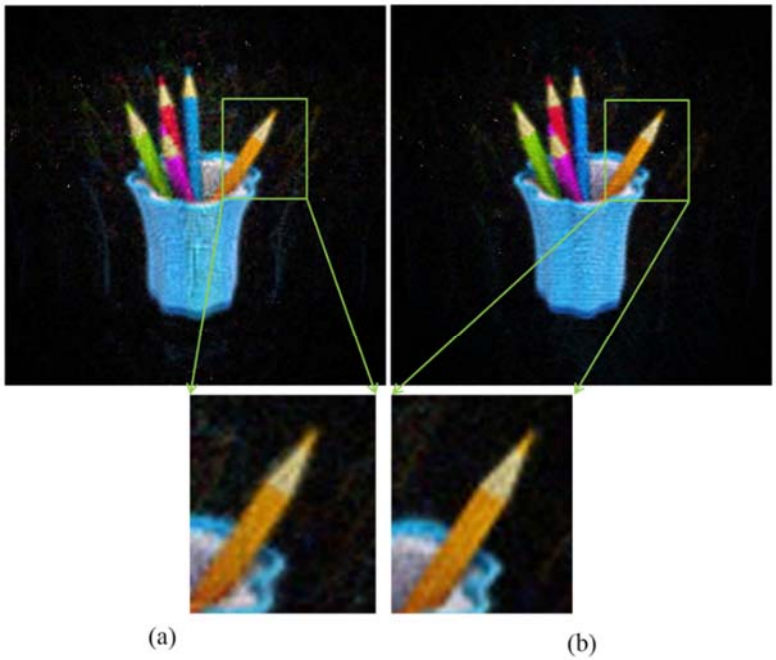

Figure 3.15. Comparison of the reconstructed image. (a) Rectangular lens array case. (b) Hexagonal lens array case.

Table 3.3 shows the parameters that are used in the simulations. We compared the reconstructed images of using a hexagonal lens array and a rectangular lens array. Figure 3.15 shows the magnified results. The images on the right side are the reconstructed images using the hexagonal lens array method and the left images are the reconstructed images using the rectangular lens array method. Aliasing happens in both cases since the elemental lens pitch p is not sufficiently small in comparison with the bandwidth of the object. As expected, due to larger maximum radial spatial frequency and the hexagonal shape of the cut-off spatial frequency region, it can be seen that there are more aliasing in the rectangular lens array case compared to the hexagonal lens array case. In order to measure the resolution improvement, I calculated the peak signal-to-noise ratio (PSNR) and normalized cross correlation (NCC) between the reconstructed images and the original image. The PSNR is defined as

$$PSNR = 10 \times \log_{10}\left(\frac{\left(2^N - 1\right)^2}{\frac{1}{MN} \sum_m \sum_n \left\| I_1(m,n) - I_2(m,n) \right\|^2} \right), \qquad (3.13)$$

and NCC is defined as

$$NCC = \frac{\sum_{m,n}\left[I_1(m,n)-\overline{I_1}(m,n)\right]\left[I_2(m,n)-\overline{I_2}(m,n)\right]}{\sqrt{\sum_{m,n}\left[I_1(m,n)-\overline{I_1}(m,n)\right]^2\left[I_2(m,n)-\overline{I_2}(m,n)\right]^2}}, \quad (3.14)$$

where I_1 and I_2 are the images to be compared, $M \times N$ are the pixel size of the images, $\overline{I_1}$ and $\overline{I_2}$ are the means of the two images. The results are shown in Table 3.3. The resolution improvement is 2.42dB for PSNR and 0.0109 for NCC.

3.2.5. Experiment results

The theory was also verified experimentally. We performed two experiments, one using rectangular lens array and the other using hexagonal lens array. The setups for capturing the elemental images are the same, as Figure 3.16 shows. The difference is only the lens array shape. Both the rectangular lens array and the hexagonal lens array have 1 mm lens pitch. The focal length of the two lens arrays is 3.3 mm. The pixel count of the elemental images along the horizontal direction is 58 pixels.

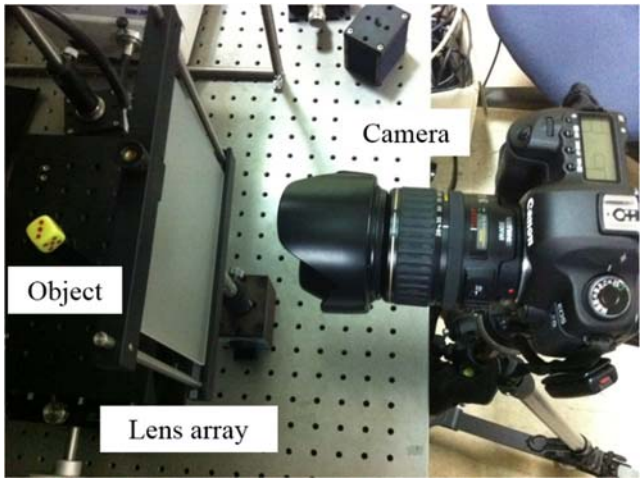

Figure 3.16. Experimental setup for capturing objects.

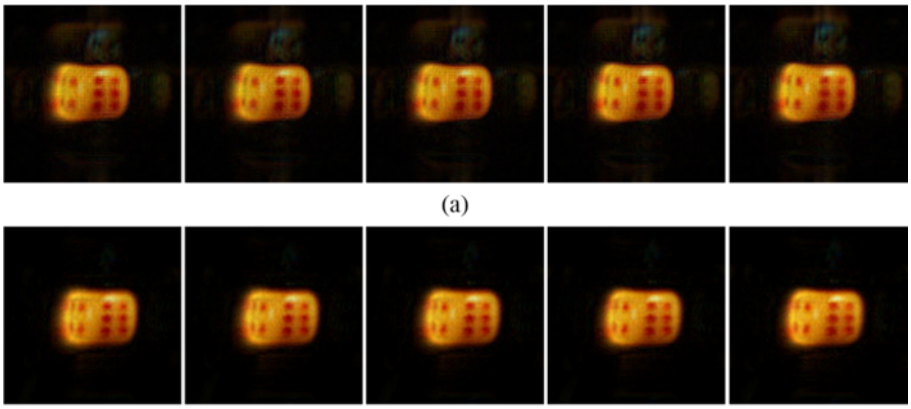

Figure 3.17. Numerical reconstruction: (a) Rectangular lens array case. (b) Hexagonal lens array case.

Figure 3.17 shows the movie snap shots of the numerical reconstruction at different distances of the generated hologram. It is obvious that the reconstructed images using hexagonal lens array show less aliasing than those using the rectangular lens array.

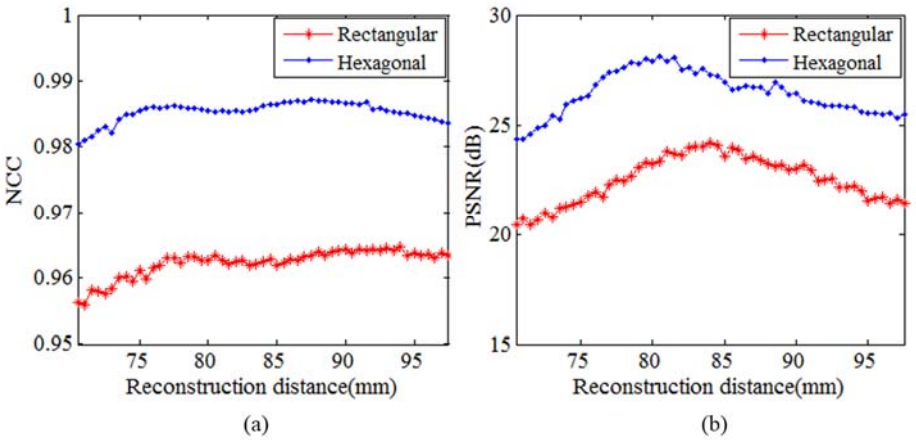

Figure 3.18. PSNR and NCC of the images reconstructed at different distances. (a) NCC and (b) PSNR.

To verify the image quality enhancement of the reconstructed images, we calculated the PSNR and NCC values. The results are shown in Figure 3.18. Figure 3.18(a) shows the PSNR of the reconstructed depth images. The average values are shown in Table 3.4. The improvement is about 3.94dB. Figure 3.18(b) shows the NCC of the reconstructed depth images. The blue-dimond and red-star lines are the NCC of reconstructed images using hexagonal lens array and rectangular lens array, respectively. The improvement of average NCC is about 0.0230.

Table 3.4. Average PSNR and NCC values of the reconstructed images

	Rectangular lens array	**Hexagonal lens array**	**Improvement**
PSNR	22.48 dB	26.42 dB	3.94 dB
NCC	0.9623	0.9853	0.0230

3.3. Chapter Summary

In this chapter, I analyzed the parameters that affect the resolution of the hologram synthesized from orthographic view images. It was found that the projection angle interval between neighboring orthographic view images determines the maximum size of the reconstruction field. It was also found that the maximum projection angle and the element lens pitch of the lens array determine the maximum spatial frequency of the reconstruction. Based on this analysis, a lens array shift method was proposed to enhance the resolution of the reconstructions. By shifting a lens array along the horizontal and vertical direction, respectively, four groups of elemental images were captured, and the orthographic images was synthesized from the four elemental images instead of only one in the conventional method. This is corresponding to sampling the object with half sampling interval and double sampling number, hence enhanced the resolution of the hologram reconstruction. Due to the efficiency of the hexagonal sampling technique, I also compared the

resolution of the Fourier hologram reconstruction methods using a rectangular lens array and a hexagonal lens array based. From the sampling theory, it showed that the resolution of the reconstruction is better in the case of using hexagonal lens array than in the case of using rectangular lens array.

All the principle and the feasibility of the proposed methods were verified numerically and experimentally. The simulation and experimental results confirmed the validity.

Chapter 4. Fourier hologram generation from three photos captured at different focal planes

4.1. Introduction

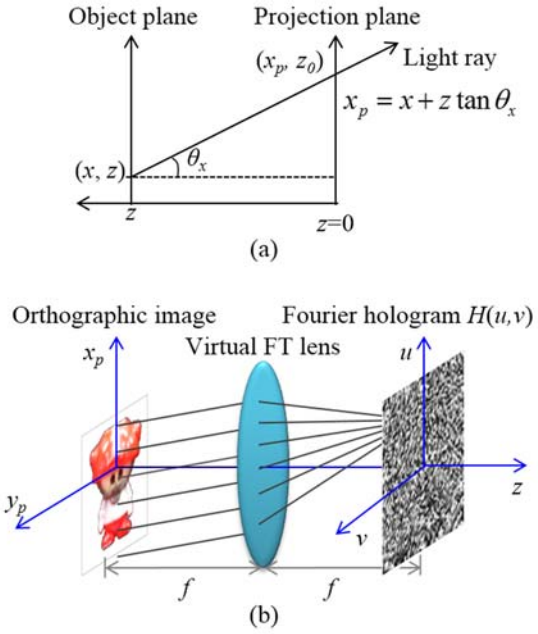

Figure 4.1. Basic idea of Fourier hologram synthesizing from orthographic images. (a) Definition of orthographic images, and (b) thin lens affection to an orthographic projection image illuminated with plane wave.

Techniques of hologram generation from multiple view images [118] have advantages over the traditional interferometry based methods. The

multiple perspective projection or orthographic projection view images are captured by multiple cameras or single camera with multiple step movement, and can also be captured simply by a single shot through a lens array. Among these methods, hologram generation from orthographic images based on lens array [59, 108] has its advantages. In this method, it performs exact Fourier hologram calculation and manipulation of the reconstructions' locations is possible. The main process is shown below.

As section 3.1 described, an orthographic view image of a 3D object is the projection of the object with a firm projection angle. The definition can be described as Figure 4.1(a), each point on one projection image $P(x_p, y_p; z)$ has the same projection angle (θ_x, θ_y). The orthographic geometry has the projection lines all parallel to each other. The projection image coordinates can be written as

$$\begin{aligned} x_p &= x + z \tan \theta_x, \\ y_p &= y + z \tan \theta_y. \end{aligned} \tag{4.1}$$

As Figure 4.1(b) shows [88], Since a thin lens transfers a plane wave focused into a point in the lens focal plane, and an orthographic image is corresponding to illuminating an object with a plane wave, the Fourier transform of a real existing object can be synthesized from the

orthographic images by doing digital lens transformation. Therefore, the Fourier hologram of a 3D object can be synthesized by integrating each of the orthographic images corresponding to each point position on the hologram. The proof is shown below [98, 99]. The mathematic representation was proved to

$$H(\xi,\eta) = \int\int P_{\xi,\eta}(x_p, y_p) \exp\left[-j2\pi B\left(\xi x_p + \eta y_p\right)\right] dx_p dy_p, \quad (4.2)$$

where B is an constant, and the value depends on how we define the projection angle of the orthographic images. In the previous method, this is defined by the parameters of the lens array.

Previous techniques gain orthographic images by using lens arrays and post digital processing [59]. The lens arrays sample the real object with less numbers and limited sampling interval. Therefore the resolution of the reconstructed images is limited. Although my previous work [95, 119] performed improvement to the resolution of the hologram reconstructions, significant improvement is impossible since there exists a mutual restriction between the pitch and number of the lens arrays. Fortunately, there are methods that I can use to obtain orthographic images without using lens arrays or multiple cameras. One technique was proposed by A. Orth, and named as light field moment imaging (LFMI). It is an equation that describes the transverse of the light filed [120]. The

following section will introduce this LFMI technique.

The light field function is a description of irradiance in the ray optics regime [121]. It describes the total geometric distribution of light as a five- or four-dimensional function which represent both spatial position and the direction of light flow. As Figure 4.2 shows, a light field $L(x; y; \tan\theta_x, \tan\theta_y; z_1)$ represents the density of rays at a point $(x, y; z_1)$, propagating in the direction specified by an angle (θ_x, θ_y). In light field imaging, both the intensity and direction of rays impinging on the image sensor are recorded [122, 123].

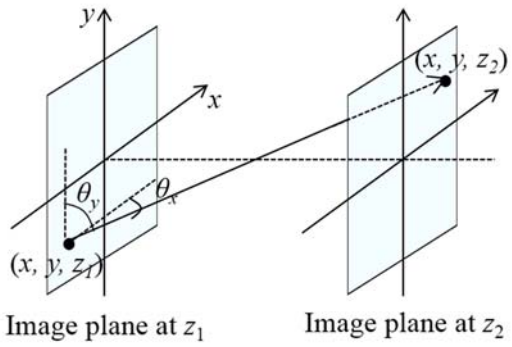

Figure 4.2. Light field definition.

The LFMI technique obtaining light field using two photographic images with a focus plane shift along the optical axis. It shows that the difference between the two images that are captured with a slightly different focal planes satisfies a Poisson equation

$$\frac{\partial I}{\partial z} = -\nabla^2{}_{\perp} U(x, y; z), \tag{4.3}$$

where ∂I and ∂z are the intensity difference and depth difference respectively, and $\nabla U(x, y; z) = I(x, y; z) M(x, y; z)$, where $M = [s(x,y;z), t(x,y;z)]$ is a vector containing the normalized first moments of the light field over its angular coordinates. By solving this equation, first moment of the light field can be obtained. Suppose the angular distribution of rays is Gaussian, the orthographic projection view images at the first image plane then can be calculated from the first moment using this equation[121, 124] of

$$\begin{aligned} &L(x, y, \tan\theta_x, \tan\theta_y; z_1) \\ &= I_2(x, y) \times \exp\left\{ -\frac{[\tan\theta_x - s(x, y)]^2 + [\tan\theta_y - t(x, y)]^2}{NA^2} \right\}, \end{aligned} \tag{4.4}$$

where NA is the numerical aperture of the optical system that is used to capture the two images. Since Eq. (4.3) is a Poisson Equation which has the same format of the transport of intensity equation, Δz in this LFMI equation can be solved by fast Fourier transform, thus the affect of Δz is the same as in the TIE. Too small Δz amplifies the noise in the capturing process much more, but too large Δz breaks down the approximation of the LFMI equation, thus blurs the images. Therefore there exists the optimal Δz. However, since the blurs in the captured images depends on

the spatial frequency components, Δz will be object dependent. This need to be further studied.

Since this technique is new, it has not been applied to applications. In this chapter, we applied this technique to Fourier hologram synthesizing from two photographic images. Since no optical components except the camera is used in the imaging system, this method does not have the limitations in the lens array based method. Thus I also compare the parameters that affect the resolutions of the hologram and the reconstructions.

4.2. Theory

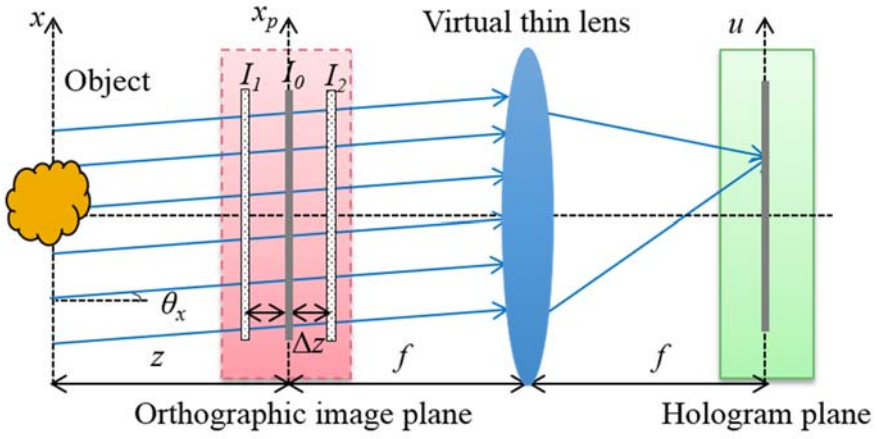

Figure 4.3. Scheme of the proposed method.

Figure 4.3. shows the one-dimensional scheme of the proposed method.

The red dashed and green solid squares are the inputs and final calculated hologram of the proposed method, respetively. The inputs are three photos of an object captured with a digital camera. The processes between the input images and the output Fourier hologram are all digitally performed. In the red area, three images $I_0 = I(x, y; z_0)$, $I_1 = I(x, y; z_1)$ and $I_2 = I(x, y; z_2)$ of an object are captured with a distance interval Δz. I_0 is located at the focal plane while I_1 and I_2 are located in front and behind the the focal plane. In this case, the left hand of Eq. (4.3), which represents the transverse light field at the position of z_0, thus can be expressed as

$$\frac{\partial I(x,y;z_0)}{\partial z_0} = \frac{I(x,y;z_2) - I(x,y;z_1)}{2\Delta z}. \tag{4.5}$$

Hence, $M(x, y; z_0) = \nabla U(x, y; z_0)/I(x, y; z_0)$, which is the the first angular moment of the light field at the focal plane of the camera. Therefre, the light field at the focal plane becomes

$$\begin{aligned} &L(x, y, \tan\theta_x, \tan\theta_y; z_0) \\ &= I(x, y; z_0) \times \exp\left\{ -\frac{[\tan\theta_x - s(x, y)]^2 + [\tan\theta_y - t(x, y)]^2}{NA^2} \right\}. \end{aligned} \tag{4.6}$$

Three photos are used to make a more practical light field transverse expression. Apart from this, in the orthographic images calculation, this

makes the the images of different depth planes have less defocus blurring.

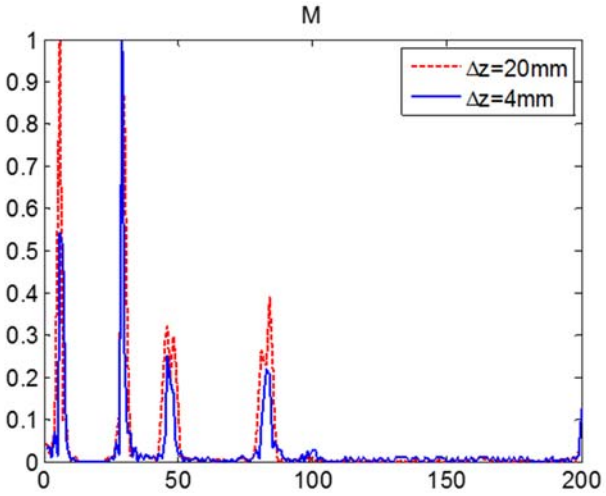

Figure 4.4. Comparison of M according to different Δz.

From the previous paragraph, I can see Δz affects $U(x, y; z_0)$, and $U(x, y; z_0)$ affects the first angular moment M of the light field. We examined how the Δz affect the M. I use two group of images with Δz= 4mm and 20mm respectively, all the other parameters are the same. I performed the process in the previous paragraph, and compared the $M[s(x, y_0; z_0)]$, where y_0 is a constant. Figure 4.4 shows the result. We can see the calculated M almost coincides with each other alrough the depth differences are different. Since M restricts the view range of the calculated perspective images, we can say that with different depth gap in the captured photos, the parrallax of the perspective view images is

not affected.

As the orthographic projection images are two-dimensional projection images of a 3D object with parallel projection lines, as the blue lines in the left of the lens in Figure 4.3, they can be calculated by integrating the light fields that have the same direction. With the LFMI technique [121, 124], orthographic projection images of an object at the focal plane of the camera can be obtained from these three photographic images. In my method, the symbol of the orthographic projection images is $P_{\xi,\eta}(x_p, y_p)$, while (x_p, y_p) is the local coordinates in one orthographic image, and (ξ, η) is the position coordinates of the orthographic images. Since there is no other optical components between the object and the orthographic images, the coordinate of the orthographic images is defined by the projection angle and the distance between the object and the camera, i.e. $\xi = z_0 \times \tan\theta_x$ and $\eta = z_0 \times \tan\theta_y$. Substituting these parameters to Eq.(4.2), we conclude that

$$B = \frac{2}{\lambda z_0}, \tag{4.7}$$

should be settled in my method to make a Fourier hologram with the previously calculated orthographic images. λ is the wavelength of the assumed plane waves used to illuminate each orthographic image in the

calculation, z_0 is the distance between the object and the orthographic image plane.

It should be noticed that the precise z_0 in the previous section is impossible to be measured. Thus we analyzed the effect of an imprecise z_0' used in the hologram calculation. Suppose $z_0' = z_0 + \delta z$ is the distance we used in the calculation, where δz is the error. With the definition of the orthographic projection coordinates Eq. (4.1), the coordinate of the orthographic images corresponding to the estimated distance z_0' is

$$\begin{aligned} x_p' &= x + z_0' \tan\theta_x \\ &= x + \delta z \cdot \tan\theta_x + z_0 \tan\theta_x \\ &= x' + z_0 \tan\theta_x, \end{aligned} \tag{4.8}$$

where $x' = x + \delta z \cdot \tan\theta_x$. This is corresponding to lateral shift of all orthographic images with a same value. However, this does not affect the shape and depth of the object [59]. Thus, we do not need to mind an imprecise distance between the object and the captured image plane.

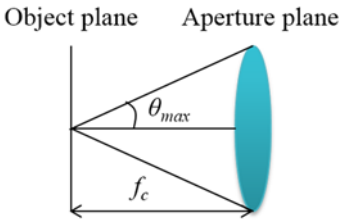

Figure 4.5. Aperture of an imaging system.

Since apart from the camera, there is no other optical components in

the imaging system, the view scope of the orthographic images is restricted by the NA of the camera in the imaging system. As Figure 4.5 shows, f_c is the focal length of the imaging lens and $\theta_{\max}$ is the maximum view angle of the imaging system. The maximum view angle of the orthographic images thus can be expressed as

$$\begin{aligned} -\arcsin(NA) \le \theta_{x\text{-max}} \le \arcsin(NA), \\ -\arcsin(NA) \le \theta_{y\text{-max}} \le \arcsin(NA). \end{aligned} \tag{4.9}$$

Suppose $N_x \times N_y$ is the number of orthographic images calculated in the digital process, and $\Delta\theta_x$ and $\Delta\theta_y$ are the projection angle interval between two adjacent orthographic images. Ideally, the smaller the ($\Delta\theta_x$, $\Delta\theta_y$), the finer the object sampling becomes and the more number of orthographic images we get. The only thing we need to do is setting the parameters of $N_x\Delta\theta_x$ within the scope of $\theta_{x\text{-max}}$ and $N_y\Delta\theta_y$ within the scope of $\theta_{y\text{-max}}$. However, the computer load in the calculating is also heavier. Thus, proper (N_x, N_y) and ($\Delta\theta_x$, $\Delta\theta_y$) should be chosen. As one orthographic image contributes to a single pixel in the hologram, $N_x \times N_y$ is also the generated hologram size.

4.3. Simulation results

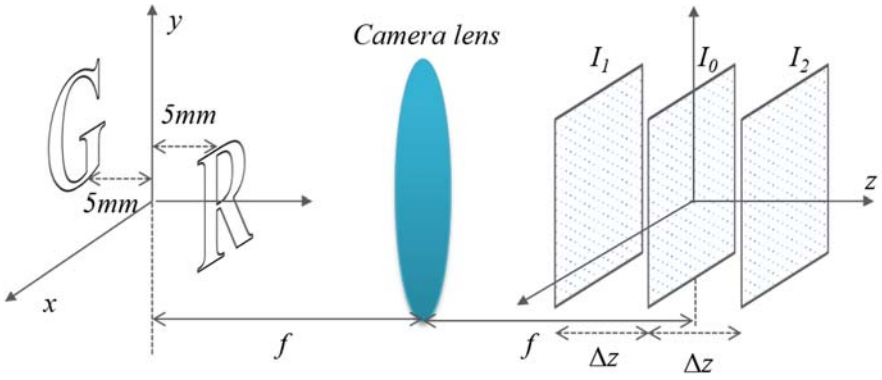

Figure. 4.6. Scheme of the simulation.

In the simulation, we used two plane images with a depth of 10mm as the object. Figure. 4.6 shows the scheme of the simulation. Each plane is 5mm away from the center depth. The center depth of the object locates at the focal plane of the camera. The NA is 0.3. The view scope along the vertical and the horizontal directions is (-8°~8°). I captured three photos of the object, i.e. I_0 , I_1 , I_2, as Figure. 4.6 shows. The distance between two adjacent photos is Δz= 5mm.

Figure. 4.7. Three photoes of the object.

Figure 4.7 shows the orthographic images viewed from top-left,

center and bottom-right at the camera sensor plane. To view the parrallax clearly, we plotted each of the images of Figure. 4.8 through the vertical and horizontal lines at the positions shown in Figure. 4.9. Figure 4.10 shows the results. It can be observed that the images viewed from the center positions (marked as green solid lines) have less error since the left and right or above and bottom parts of the object are viewed from the same distance. For the images viewed from the other projection angles (Red dashed lines: from the left-above view point, and blue dot lines: from the right-bottom view point), we can see blurs since the view distances changed because of the different view angles. This example verifies the parrallax of the calculated orthographic images.

Figure. 4.8. Selected orthographci images.

Figure. 4.9. Reference lines for display the parallax.

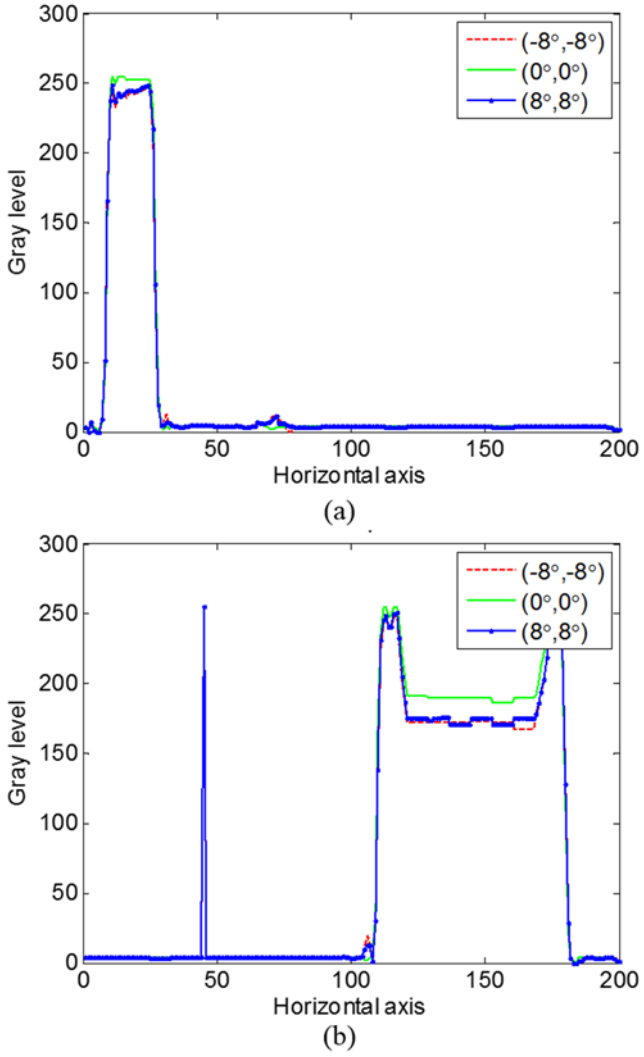

Figure. 4.10. Plot images of Figure. 4.8 along the (a) horizontal and (b) vertical line positions that are shown in Figure. 4.9.

With the number of 100×100 orthographic images, the synthesized Fourier hologram looks like Figure 4.11. Figure 4.12 shows the reconstructed plane images from Figure 4.11. To see the blur of the

images clearly, we plotted the center lines across the "G" and "R" letters in the three images located at *f*-5mm, *f*+0mm, and *f*+5mm, respectively. Figures 4.13(a) and 4.13(b) show the results for "G" and "R" respectively. Figure 4.13(c) and (d) are the magnified images of areas in Figures 4.13(a) and 4.13(b) that marked with dashed squares. The gray of the plotted images reflects the blur of the images. According to this, we can see the "G" letter focuses at the plane located at *z*=*f*-5mm and the "R" letter focuses at the plane located at *z*=*f*+5mm.

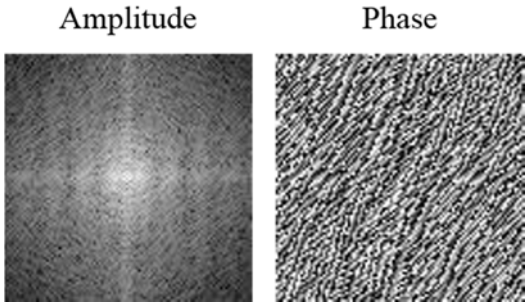

Figure 4.11. Synthesized Fourier hologram.

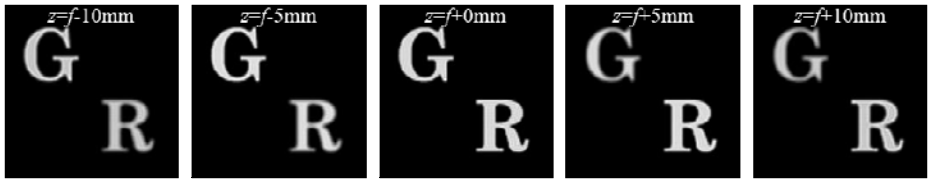

Figure 4.12. Reconstructed plane images from Figure 4.11.

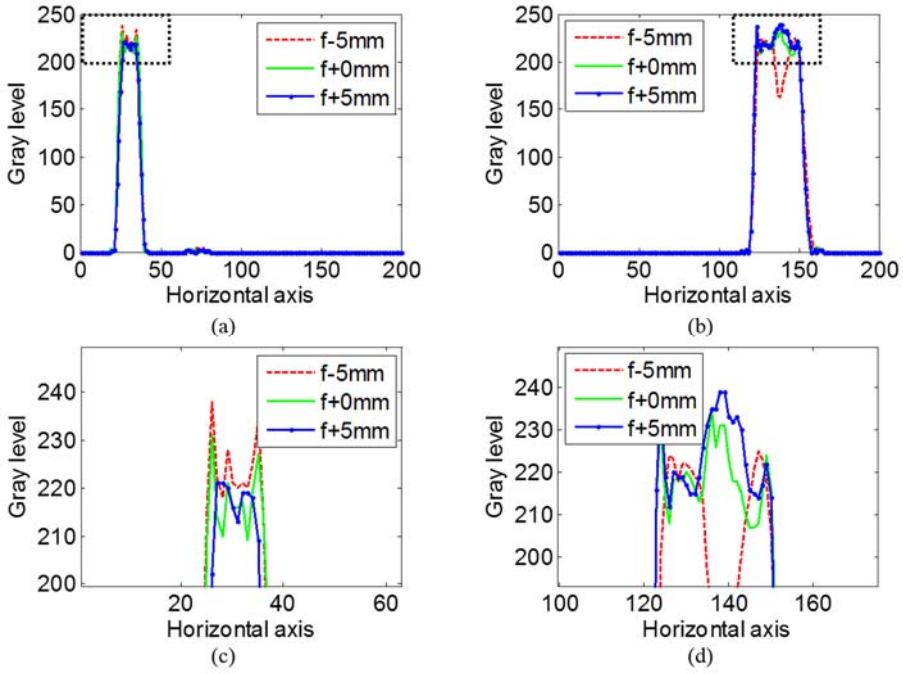

Figure 4.13. Plot images across the center of the two letters in Figure 4.12: (a), (b) Ploted images across the "G" and "R" letters, and (c), (d) magnified images of the square dashed areas in (a) and (b).

4.4. Experiment results

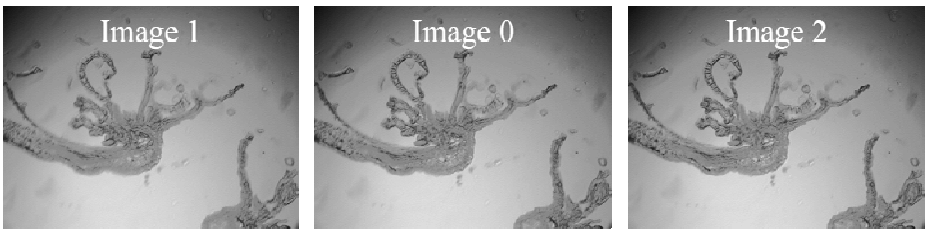

Figure 4.14. Two photos of a Pteridium Sporangia microscopy object captured at two different focal planes.

Due to the convenience of the microscopy which is very suitable to

recording focal stacks of images, I captured two images of a Pteridium Sporangia microscopy object with a 10×0.3NA objective and a charge-coupled device (CCD). Figure 4.14 shows the three captured images, the blur at the center part is obvious for image 1 but not in image 2. The numerical aperture gives a view angle about -17°~17°. From the two images, 200(H)×200(V) orthographic images were calculated with an angular interval of 0.15°(H)×0.15°(V), while in this case the view angle of the reconstructed images should be -15°~15°, which is in the scope of the maximum view angle of the system. The resolution of the orthographic images is 2336×1752 and the pixel pith is 5.5μm, both of them are the as the directly captured images. Figure 4.15 shows three selected orthographic images of the object with vertical parallax.

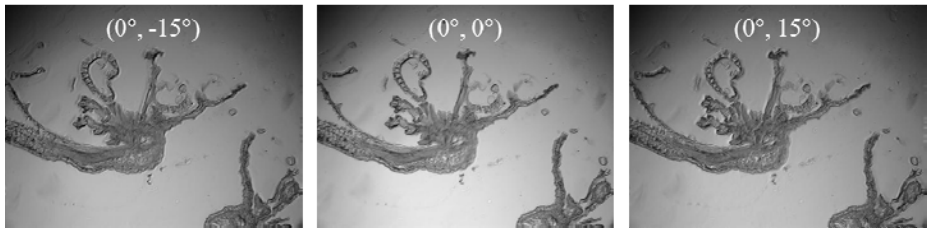

Figure 4.15. Selected orthographic images of the object.

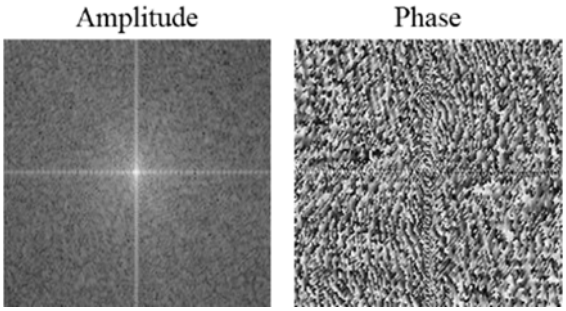

Figure 4.16. Synthesized Fourier hologram.

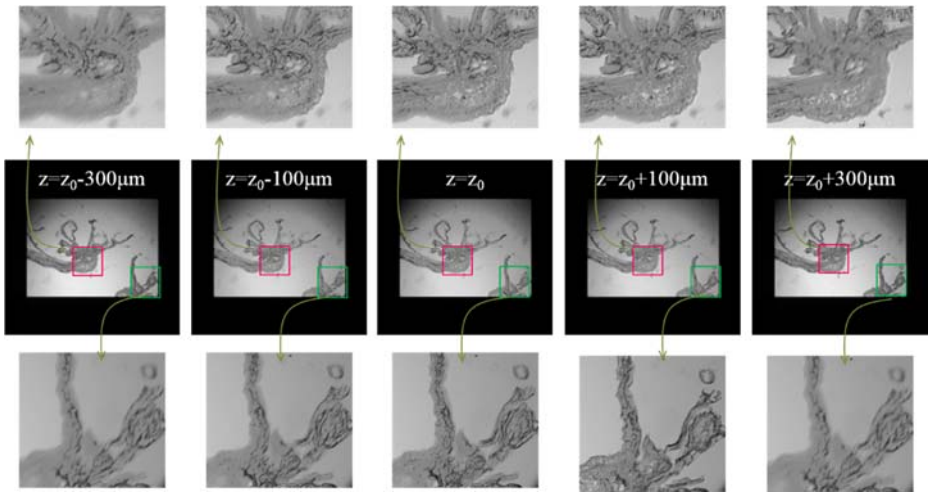

Figure 4.17. Reconstructed plane images along the optical axis.

The synthesized amplitude and phase profiles of the the Fourier hologram are shown in Figure 4.16. In the hologram synthesizing, we suppose the distance between the object and the first image plane is 50mm. Figure 4.17 shows the reconstructed images along the optical axis. The images in the first line show the corresponding magnification of the areas that are resolved by the red squares in each of the reconstructed

images on the center line, and the images on the third line are the magnification of areas that are resolved by the green squares. From the first and third lines, we can see that the center part of the reconstructed object is focused on the second image, and the right bottom part of the reconstructed object is focused on the fourth image. This experimental result shows different parts of the reconstructed object focused at different planes.

Figure 4.18. Two photos of a book cover captured at two different focal planes.

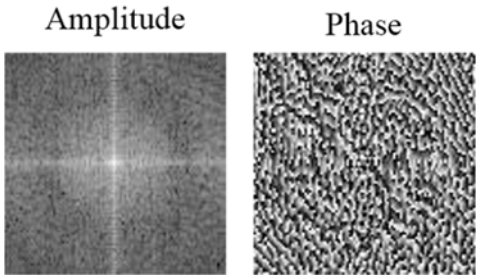

Figure 4.19. Synthesized Fourier hologram.

We also did experiment using a large general object. Since it is not easy to capture three photos to get the transverse light field at the center plane, two photos were used to give an estimated transverse light field at

the first image plane. The book of "Introduction to Fourier Optics" was tilted on a desk, where the beginning letters of the title are farther than the ending letters. Two captured images were focused on the distant parts and the near parts of the title respectively. Cannon EOS 5D Mark II was used to capture the images with f/2.8. The view scope of the imaging system is about -10.3°~10.3°. Figure 4.18 shows the two captured images, and Figure 4.19 shows the Fourier hologram synthesized from 100×100 number of orthographic images. Figure 4.20 shows the reconstructed images located at different planes along the optical axis, from which different parts located at different planes can be observed. However, the results look different from the real object, because the orthographic images calculated at the first image plane do not have the average amount of focus/defocus for all the parts of the object. In addition, the tranverse of the light field at the first image plane just estimated by two photos is not enough. This problem needs further study.

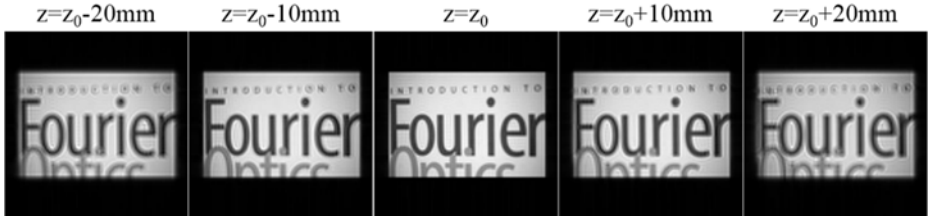

Figure 4.20. Reconstructed plane images along the optical axis.

By now, the first experimental result verified the feasibility of microscopy reconstruction and the second one verified the feasibility of general size object reconstruction by using the proposed method.

I also show the comparison between the conventional method and the proposed method. Here the conventional method is the lens array based Fourier hologram synthesis method improved by a lens array shift approach. We suppose a lens array that has a focal length of 3.3mm and a lens pitch of 1mm (general lens array used in the previous work). In the conventional method, the view scope is depending on the focal length and lens pitch of the lens array, it is about -8°~ 8°. Since the pixel count of one elemental image is limited by the lens pitch of the lens array and the pixel pitch of the camera sensor, it is 100×100 pixels even with the lens array shift method which doubles the pixel count of one elemental image. Therefore, the projection angle interval becomes about 0.17°. In the proposed method, the *NA* of the camera limits the view scope, smaller the *NA*, larger the view scope. As in the first experiment of the proposed method, the view scope is -15°~15°. I choose the projection angle interval 0.15° , thus the pixel number of the hologram is 200×200. Ideally, it is possible to be smaller for the projection angle interval and larger for the hologram resolution. But we need to notice the parrallax

between two orthographic images reduces as the projection angle interval becomes smaller. In addition, too small parralllax of the orthographic images contributes nothing to the hologram. Therefore, even though we can produce as much as possible orthographic images (as smaller as possible projection angle interval), it just gives more pixels to the hologram but does not make sense. Anyway, the limitations induced by the lens array do not appear in our proposed method; this is the main advantage of the proposed method.

4.5. Chapter summary

We developed hologram generation from three photographic images captured with a slight depth difference. We used the three photos to create orthographic images without sampling limitations induced by other optical components, for example the lens array. Therefore, we can synthesize higher resolution holograms. Since synthesis of the orthographic images was from the conventional photos, the object size can be from microscopy to general objects. With the simplicity of the capturing, we can achieve real-time hologram generation if we apply parallel computing in the hologram calculation.

Chapter 5. Conclusion

This thesis has worked on optical imaging with the multiple diffracted intensity images or photographic images. Optical imaging with iterative calculation that is applied to multiple intensity images captured under coherent illumination has its limitations: the convergence is slowly and the coherence induces speckles. The slow convergence of the calculation should be improved with the intensity image capturing or the computer algorithm. Also, the limitations from coherent illumination needs to be removed. Fortunately, holograms synthesis from multiple view images is one approach. In the research of synthesizing hologram from multiple view images, the main issue is how to recording the multiple view images. Lens array has been widely used to capture multiple view images with one single shot. However, the lens array samples the real object insufficiently. Therefore, multiple view images captured with simple experimental setups and without lens needs to be used. All the works I have done were about the above issues, and I briefly summarize them as below.

The work of Chapter 2 showed an algorithm for performing fast convergence in wavefront reconstruction from multiple diffracted

intensity measurements. By resampling captured diffractive intensity images with different levels, images representing high resolution and low resolution components of an object can be separated. Thus, different number of iterations can be applied to the resampled images respectively. It therefore shows fast convergence in the iterative phase reconstruction. Both simulated and experimental results have shown the convergence of the proposed method was about two times faster than the conventional method for the case of test images.

The general recording of multiple view images is always bulky or introduces sampling problems. Therefore, I had proposed the lens array shift method. However, in this method, I had introduced movement to perform the shifting of the lens arrays and sacrificed the simplicity of the capture. Thus, hexagonal lens array instead of rectangular lens array was recommended to producce more efficient sampling strategy and thus get better hologram reconstruction. The work of Chapter 3 gave a resolution comparison of hologram reconstruction between using rectangular and hexagonal lens arrays. It showed that capturing multiple view images using hexagonal lens array produces higher resolution in the hologram reconstruction. However, both lens array shift method and hexagonal lens array cannot reach significant improvement in the hologram

reconstruction, this is due to not enough sampling from the lens array. Thus I proposed a method for synthesizing hologram without a lens array in the capturing.

Chapter 4 developed a hologram synthesizing method from three photographic images captured with sunlight illumination and a general camera. The three images are located along the optical axis and with a slight depth difference. With the three images, we can get orthographic images using the light field moment imaging technique. Since the limitations introduced by the lens array in the conventional method do not exist, higher resolution holograms can be synthesized, and the object size is only limited by the camera. With the simplicity of the capture, we can achieve real-time hologram generation if we apply parallel computing in the hologram calculation.

Appendix A

Here, I analyze both the maximum size of the hologram reconstruction and its maximum spatial frequency. For the maximum size of the reconstruction, I found that the main factor is the interval of the orthographic projection angle. Too large a projection angle interval causes overlapping in the reconstruction. For the maximum spatial frequency, there are three factors that affect it, i.e., the capturing lens array pitch, the maximum orthographic projection angle, and the spatial frequency bandwidth of the object. The dominant factor is determined by the relationship among these three factors. The computational results are presented to verify the parameter analysis.

A.1. Relations between optical fields at different planes

Generally, a 3D object can be written as

$$O(x, y, z) = \sum_{z_0} O(x, y; z_0)\delta(z - z_0), \tag{A.1}$$

where $O(x, y; z_0)$ represents a slice of the 3D object at $z=z_0$, and δ is the Dirac delta impulse function. Hereafter we only consider the object slice $O(x, y; z_0)$. Since the generated 3D object can be regarded as a collection of these slices, as represented in Eq. (A.1), the analysis presented in the following sections can be applied to each slice of the object, enabling

estimation of the reconstruction quality of the 3D object. The Fourier hologram of the object slice $O(x, y; z_0)$ is given by [4]

$$H(u,v) = \exp\left[-j\frac{z_0\pi}{\lambda f^2}\left(u^2+v^2\right)\right] \times \iint O(x,y;z_0)\exp\left[j\frac{2\pi}{\lambda f}\left(xu+yv\right)\right]dxdy, \tag{A.2}$$

where f is the focal length of the Fourier transform lens and λ is the wavelength. The Fourier transform of the Fourier hologram $H(u, v)$ given by Eq.(A.3) is

$$\begin{aligned} & FT\{H(u,v)\} \\ &= FT\left\{\exp\left[-j\frac{z_0\pi}{\lambda f^2}\left(u^2+v^2\right)\right]\right\} \\ &\quad \otimes FT\left\{\iint O(x,y;z_0)\exp\left[j\frac{2\pi}{\lambda f}(xu+yv)\right]dxdy\right\} \\ &= \exp\left[-j\frac{\pi}{\lambda z_0}\left(x^2+y^2\right)\right]\otimes O(x,y;z_0) \\ &= \iint O(x,y;z_0)\exp\left[-j\frac{\pi}{\lambda z_0}\left((x-\xi)^2+(y-\eta)^2\right)\right]dxdy, \end{aligned} \tag{A.3}$$

where the constant phase factor is ignored. The last expression of Eq. (A.3) is the Fresnel propagation of the object slice over a distance z_0. Therefore we can see that the Fourier transform of the Fourier hologram $H(u, v)$ is the object field of the object slice at $z=z_0$ plane propagated to $z=0$ plane.

From the above discussion, the process of 3D Fourier hologram generation and reconstruction can be represented by Figure A.1 [59]. It can be divided into several steps. First, the object field $O(x, y; z_0)$ is propagated to z=0 plane $O_z=O(\xi, \eta)$. The integral Fourier hologram $H(u, v)$ can be thought as a Fourier transform of $O_z=O(\xi, \eta)$. In the reconstruction, by Fourier transform the hologram $H(u, v)$ and the object field at z=0 plane, $O'_{z=0}(\xi', \eta')$ can be obtained. The integral Fourier hologram $H(u, v)$ can be thought as a Fourier transform of $O_{z=0}(\xi, \eta)$. In the reconstruction, by Fourier transform the hologram $H(u, v)$, the object field $O'_{z=0}(\xi', \eta')$ at z=0 plane can be obtained. Finally the object slice $O'(x', y'; z_0)$ can be reconstructed by Fresnel propagating $O'_{z=0}(\xi', \eta')$ over a distance z_0.

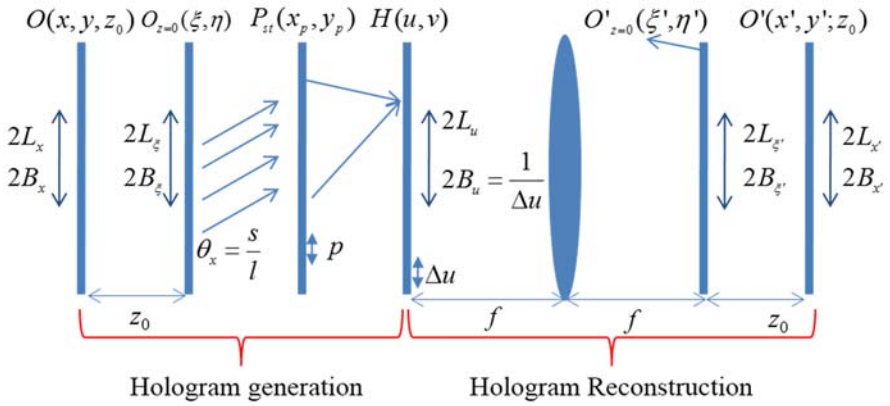

Figure A.1. Scheme of the Fourier hologram generation from orthographic projection images.

Suppose the object $O(x, y; z_0)$ has lateral size $2L_x \times 2L_y$ and bandwidth $2B_x \times 2B_y$. The object optical field $O_{z=0}(\xi, \eta)$ at $z=0$ plane can be calculated by Fresnel propagating the object over distance z_0. The size of the object field at $z=0$ plane is given by $2L_\xi = 2L_x + 2B_x \cdot \lambda \cdot z_0$ and the bandwidth is maintained at $z=z_0$ plane, i.e., $2B_\xi = 2B_x$ [125, 126].

A.2. Overlapping in the space domain of the reconstructions

Figure A.2 shows the space domain representation of the object optical field at $z=z_0$ and $z=0$ planes. The object field at $z=0$ plane is obtained by Fresnel propagating the object field at $z= z_0$ plane over distance z_0. In the reconstruction, the object optical field $O'_{z=0}(\xi', \eta')$ at $z=0$, is obtained by taking Fourier transform of the hologram[4]. The repetition period of the reconstructed objects at $z=0$ plane is given by $\lambda f/\Delta u = \lambda/2\Delta\theta$.

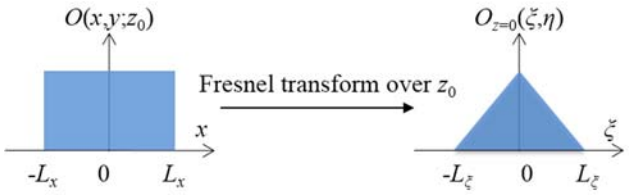

Figure A.2. Space domain representation of the object field at $z=z_0$ and $z=0$ plane.

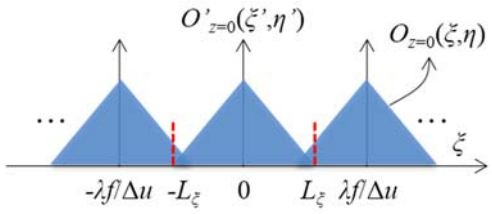

Figure A.3. Space domain representation of the reconstruction at z=0 plane.

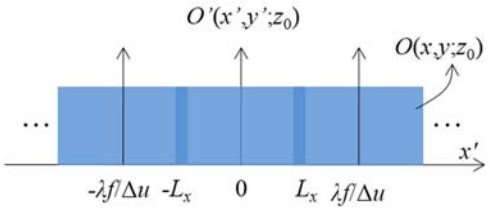

Figure A.4. Space domain representation of the reconstructed object at $z=z_0$ plane.

Figure A.4 is the final reconstruction $O'(x', y'; z_0)$ at $z=z_0$ plane. This is obtained by taking Fresnel transform to $O'_{z=0}(\xi', \eta')$ over a distance z_0. From Figure A.4, we can see that if we want to reconstruct the object without overlapping, inequality (A.4) must be satisfied. Following inequality (A.4), the projection angle interval $\Delta\theta$ should be controlled to prevent overlapping of the reconstructed object.

$$L_x \le \frac{\lambda f}{2\Delta u} = \frac{\lambda}{4\Delta\theta}. \qquad \text{(A.4)}$$

A.3. Spatial frequency of the reconstructions

Figure A.5 shows the spatial frequency domain representation of the object at $z= z_0$ and $z=0$ plane. The bandwidth of the object is maintained after Fresnel propagation over distance z_0 [125, 126].

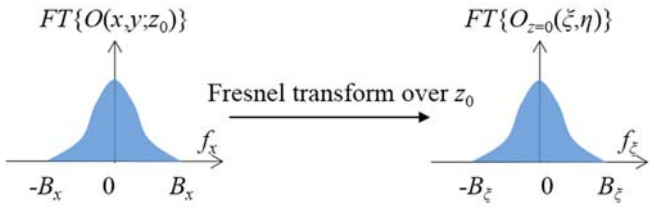

Figure A.5. Spatial frequency domain representation of the object at $z= z_0$ and $z=0$ planes.

The main factors determining the resolution of the reconstruction are elemental lens pitch p and the maximum projection angle θ_{max}. In the integral Fourier hologram generation process, orthographic view images that are synthesized by collecting the pixels from every elemental image are used. Since only one pixel is extracted from each element image, the spatial sampling interval of the orthographic view image is given by the element lens pitch p. The 3D object is first sampled with p in the orthographic view synthesis, and the orthographic view images are used in the hologram generation. Hence the reconstruction of the hologram reflects this sampling effect as a repetition of the original object field with $1/p$ period in the spatial frequency domain. Another factor that determines the reconstruction resolution is the maximum projection

angle θ_{max}. As discussed in previous section, the half size of the hologram L_u is determined by the maximum projection angle θ_{max} as $L_u=2f\theta_{max}$. According to the sampling theorem, the maximum frequency of the reconstructed object from the Fourier hologram is given by [4],

$$f_{x',max}=f_{\xi',max}=\frac{L_u}{\lambda f}=\frac{2\theta_{max}}{\lambda}. \tag{A.5}$$

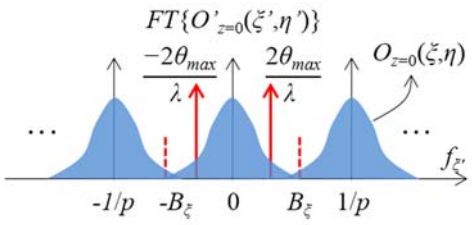

Figure A.6. Spatial frequency domain representation of the reconstruction at z=0 plane.

Figure A.6 shows the spatial frequency domain representation of the reconstructed field at z=0. From Figure A.6, it is obvious that in order to avoid aliasing in the reconstruction, the bandwidth of the object should be smaller than the sampling rate of the object, i.e.,

$$B_x = B_\xi \le \frac{1}{2p}. \tag{A.6}$$

Figure A.7 is spatial frequency domain representation of the reconstructed object at $z=z_0$. The maximum frequency is limited by the maximum projection angle in the element image capturing process and

the wavelength in the hologram calculation. If we want to reconstruct the object without high frequency loss, assuming that there is no aliasing, the cutoff frequency $2\theta_{max}/\lambda$ must be larger than the bandwidth of the object,

$$B_x < \frac{2\theta_{\max}}{\lambda}. \tag{A.7}$$

If there is aliasing, however, we need to make the cutoff frequency as large as possible while rejecting the aliased frequency region. The condition is given by

$$\frac{2\theta_{\max}}{\lambda} < \frac{1}{p} - B_x. \tag{A.8}$$

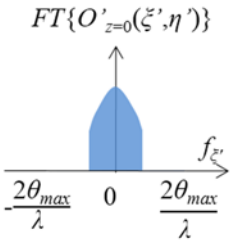

Figure A.7. Spatial frequency domain representation of the final reconstruction at $z=z_0$ plane.

Appendix B

Portions of the work discussed in each chapter of this thesis are also presented in the following publications:

[Chapter 2] N. Chen, J. Yeom, K. Hong, G. Li, and B. Lee, "Fast convergent algorithm for wavefront reconstruction based on a sequence of diffracted intensity images," Journal of Optical Society of Korea, vol. 18, no. 3, 2014.

[Chapter 3] N. Chen, J. Yeom, J.-H. Jung, J.-H. Park, and B. Lee, "Resolution comparison between integral imaging based hologram synthesis methods using rectangular and hexagonal lens arrays," Optics Express, vol. 19, no.27, pp. 2152-2167, 2011.

[Appendix A] N. Chen, J.-H. Park and N. Kim, "Parameters Analysis of Integral Fourier Hologram and its Resolution Enhancement," Optics Express, vol. 18, no. 3, pp. 2152-2167, 2010.

Bibliography

1. E. Wolf, "Three-dimensional structure determination of semi-transparent objects from holographic data," *Opt. Commun.* **1**, 153–156 (1969).
2. J. H. Bruning, D. R. Herriott, J. E. Gallagher, D. P. Rosenfeld, A. D. White, and D. J. Brangaccio, "Digital wavefront measuring interferometer for testing optical surfaces and lenses," *Appl. Opt.* **13**, 2693–2703 (1974).
3. D. Gabor, "A new microscopic principle," *Nature* **161**, 777 (1948).
4. J. W. Goodman, *Introduction to Fourier Optics*, 3rd ed. (Roberts & Company Publishers, Greenwood Village, 2005).
5. E. N. Leith and J. Upatnieks, "Reconstructed wavefronts and communication theory," *J. Opt. Soc. Am.* **52**, 1123 (1962).
6. J. Schmit and K. Creath, "Fast calculation of phase in spatial n-point phaseshifting techniques," in *SPIE* **2544**, M. Kujawinska, R. J. Pryputniewicz, and M. Takeda, Eds.. (1995).
7. J. E. Millerd, N. J. Brock, J. B. Hayes, M. B. North-Morris, M. Novak, and J. C. Wyant, "Pixelated phase-mask dynamic interferometer," in *SPIE* **5531**, K. Creath and J. Schmit, Eds., (2004).
8. B. T. Kimbrough, "Pixelated mask spatial carrier phase shifting interferometry algorithms and associated errors," *Appl. Opt.* **45**, 4554–4562 (2006).
9. L.-M. Stadler, C. Gutt, T. Autenrieth, O. Leupold, S. Rehbein, Y. Chushkin and G. Grübel, "Hard X ray holographic diffraction imaging," *Phys. Rev. Lett.* **100**, 245503 (2008).
10. M. Born and E. Wolf, *Principles of Optics*, Seventh (Cambridge University Press, Cambridge, 1999).

11. B. Platt, “History and principles of Shack-Hartmann wavefront sensing,” *J. Refract. Surg.* **17**, S573–7 (2001).

12. R. W. Gerchberg and W. O. Saxton, “A practical algorithm for the determination of phase from image and diffraction plane pictures,” *Optik (Stuttg)*. **35**, 237–246 (1972).

13. J. Fienup, “Reconstruction of an object from the modulus of its Fourier transform,” *Opt. Lett.* **3**, 27 (1978).

14. J. R. Fienup, “Phase retrieval algorithms: a comparison,” *Appl. Opt.* **21**, 2758–2769 (1982).

15. J. N. Cederquist, J. R. Fienup, C. C. Wackerman, S. R. Robinson, and D. Kryskowski, “Wave-front phase estimation from Fourier intensity measurements,” *J. Opt. Soc. Am. A* **6**, 1020 (1989).

16. R. Rolleston and N. George, “Image reconstruction from partial Fresnel zone information.,” *Appl. Opt.* **25**, 178 (1986).

17. R. Rolleston and N. George, “Stationary phase approximations in Fresnel-zone magnitude-only reconstructions,” *J. Opt. Soc. Am. A* **4**, 148–153 (1987).

18. B. H. Dean and C. W. Bowers, “Diversity selection for phase-diverse phase retrieval.,” *J. Opt. Soc. Am. A.* **20**, 1490–1504 (2003).

19. S. C. Mayo, P. R. Miller, S. W. Wilkins, T. J. Davis, D. Gao, T. E. Gureyev, D. Paganin, D. J. Parry, A. Pogany, and A. W. Stevenson, “Quantitative X-ray projection microscopy: phase-contrast and multi-spectral imaging,” *J. Microsc.* **207**, 79–96 (2002).

20. A. Devaney and R. Chidlaw, “On the uniqueness question in the problem of phase retrieval from intensity measurements,” *J. Opt. Soc. Am. A*. **01**, 1352–1354 (1978).

21. J. Fienup, “Reconstruction of a complex-valued object from the modulus

of its Fourier transform using a support constraint," *J. Opt. Soc. Am. A.* **4**, 118–123 (1987).

22. L. J. Allen, and M. P. Oxley, "Phase retrieval from series of images obtained by defocus variation," *Opt. Commun.* **199**, 65–75 (2001).

23. L. Allen, H. Faulkner, K. Nugent, M. Oxley, and D. Paganin, "Phase retrieval from images in the presence of first-order vortices," *Phys. Rev. E* **63**, 037602 (2001).

24. H. I. Campbell, S. Zhang, A. H. Greenaway, and S. Restaino, "Generalized phase diversity for wave-front sensing," *Opt. Lett.* **29**, 2707–2709 (2004).

25. M. R. Teague, and M. R. Teague, "Deterministic phase retrieval: a Green's function solution," *J. Opt. Soc. Am.* **73**, 1434 (1983).

26. N. Streibl, "Phase imaging by the transport equation of intensity," *Opt. Commun.* **49**, 6–10 (1984).

27. M. R. Teague, "Image formation in terms of the transport equation," *J. Opt. Soc. Am. A* **2**, 2019 (1985).

28. K. A. Nugent, D. Paganin, and T. E. Gureyev, "A phase odyssey," *Phys. Today* **54**, 27 (2001).

29. E. D. Barone-Nugent, A. Barty, and K. A. Nugent, "Quantitative phase-amplitude microscopy I: optical microscopy," *J. Microsc.* **206**, 194–203 (2002).

30. D. Paganin, and K. A. Nugent, "Noninterferometric phase imaging with partially coherent light," *Phys. Rev. Lett.* **80**, 2586–2589 (1998).

31. A. Barty, K. A. Nugent, D. Paganin, and A. Roberts, "Quantitative optical phase microscopy," *Opt. Lett.* **23**, 817–819 (1998).

32. A. W. Lohmann, "Wavefront Reconstruction for Incoherent Objects," *J.*

Opt. Soc. Am. **55**, 1555 (1965).

33. G. Stroke, and R. Restrick, "Holography with spatially noncoherent light," *Appl. Phys. Lett.* **7**, 229 (1965).

34. H. R. Worthington, "Production of holograms with incoherent illumination," *J. Opt. Soc. Am* **56**, 1397–1398 (1966).

35. G. Cochran, "New method of making Fresnel transforms with incoherent light," *J. Opt. Soc. Am.* **56**, 1513–1517 (1966).

36. G. Sirat, and D. Psaltis, "Conoscopic holography," *Opt. Lett.* **10**, 4 (1985).

37. A. S. S. Marathay, "Noncoherent-object hologram: its reconstruction and optical processing," *J. Opt. Soc. Am. A* **4**, 1861 (1987).

38. T.-C. Poon, and K. B. Doh, "Three-dimensional microscopy by optical scanning holography," *Opt. Eng.* **34**, P. Ferraro, A. Wax and Z. Zalevsky, Eds., 1338 (Springer Berlin Heidelberg, Berlin, Heidelberg, 1995).

39. G. Indebetouw, P. Klysubun, T. Kim, and T. Poon, "Imaging properties of scanning holographic microscopy," *J. Opt. Soc. Am. A*.**17**, 380–390 (2000).

40. B. W. Schilling, T.-C. Poon, G. Indebetouw, B. Storrie, K. Shinoda, Y. Suzuki, and M. H. Wu, "Three-dimensional holographic fluorescence microscopy," *Opt. Lett.* **22**, 1506 (1997).

41. L. Mertz, and N. Young, "Fresnel transformations of images," in *SPIE milestone Ser. ms*, (1996).

42. J. Rosen, and G. Brooker, "Digital spatially incoherent Fresnel holography," *Opt. Lett.* **32**, 912–914 (2007).

43. J. Rosen, G. Brooker, G. Indebetouw, and N. T. Shaked, "A review of incoherent digital Fresnel holography," *J. Hologr. Speckle* **5**, 124–140

(2009).

44. J. Rosen, and G. Brooker, "Non-scanning motionless fluorescence three-dimensional holographic microscopy," *Nat. Photonics* **2**, 190–195 (2008).

45. "Fluorescence incoherent color holography," *Opt. Express* **15**, 2244–2250 (2007).

46. P. Hariharan, *Optical Holography: Principles, Techniques and Applications*, Second, P. L. Knight, and A. Miller, Eds. (Cambridge University Press, Cambrige, 1996).

47. T. Poon, "Holography: scan-free three-dimensional imaging," *Nat. Photonics* **2** (2008).

48. Y. Li, D. Abookasis, and J. Rosen, "Computer-generated holograms of three-dimensional realistic objects recorded without wave interference," *Appl. Opt.* **40**, 2864 (2001).

49. D. Abookasis and J. Rosen, "Computer-generated holograms of three-dimensional objects synthesized from their multiple angular viewpoints," *J. Opt. Soc. Am. A* **20**, 1537–1545 (2003).

50. Y. Sando, M. Itoh, and T. Yatagai, "Holographic three-dimensional display synthesized from three-dimensional fourier spectra of real existing objects," *Opt. Lett.* **28**, 2518–2520 (2003).

51. Y. Sando, M. Itoh, and T. Yatagai "Full-color computer-generated holograms using 3-D Fourier spectra," Opt. Express 12, 6246–6251 (2004).

52. D. Abookasis, J. Rosen, Y. Sando, M. Itoh, and T. Yatagai, "Three types of computer-generated hologram synthesized from multiple angular viewpoints of a three-dimensional scene," *Appl. Opt.* **45**, 6533–6538 (2006).

53. B. Wilburn, "High-performance imaging using arrays of inexpensive

cameras" Ph.D. thesis, (Stanford University, 2005).

54. N. T. Shaked, J. Rosen, and A. Stern, "Integral holography: white-light single-shot hologram acquisition," *Opt. Express* **15**, 5754–5760 (2007).

55. S. Jung, J. Park, H. Choi, and B. Lee, "Viewing-angle-enhanced integral three-dimensional imaging along all directions without mechanical movement," *Opt. Express* **11**, 1346–1356 (2003).

56. B. Lee, S. Jung, and J.-H. Park, "Viewing-angle-enhanced integral imaging by lens switching," *Opt. Lett.* **27**, 818–820 (2002).

57. B. Katz, N. Shaked, and J. Rosen, "Synthesizing computer generated holograms with reduced number of perspective projections," *Opt. Express* **15**, 13250–13255 (2007).

58. N. T. Shaked and J. Rosen, "Modified Fresnel computer-generated hologram directly recorded by multiple-viewpoint projections," *Appl. Opt.* **47**, 21–27 (2008).

59. J.-H. Park, M.-S. Kim, G. Baasantseren, and N. Kim, "Fresnel and Fourier hologram generation using orthographic projection images," *Opt. Express* **17**, 6320–6334 (2009).

60. N. T. Shaked, B. Katz, and J. Rosen, "Fluorescence multicolor hologram recorded by using a macrolens array," *Opt. Lett.* **33**, 1461–1463 (2008).

61. N. T. Shaked and J. Rosen, "Multiple-viewpoint projection holograms synthesized by spatially incoherent correlation with broadband functions.," *J. Opt. Soc. Am. A* **25**, 2129–2138 (2008).

62. N. T. Shaked, G. Segev, and J. Rosen, "Three-dimensional object recognition using a quasi-correlator invariant to imaging distances," *Opt. Express* **16**, 17148–17153 (2008).

63. T. Mishina, M. Okui, and F. Okano, "Calculation of holograms from elemental images captured by integral photography," *Appl. Opt.* **45**, 4026

(2006).

64. D. C. Youla, and H. Webb, “Image restoration by the method of convex projections: part 1 theory,” *IEEE Trans. Med. Imaging* **1**, 81–94 (1982).

65. E. N. Leith, and J. Upatnieks, “Wavefront reconstruction with continuous-tone objects,” *J. Opt. Soc. Am.* **53**, 1377 (1963).

66. T. M. Kreis, and P.O.J. Werner, “Suppression of the dc term in digital holography,” *Opt. Eng.* **36**, 2353–2361 (1997).

67. M. R. Teague, “Irradiance moments: their propagation and use for unique retrieval of phase,” *J. Opt. Soc. Am.* **72**, 1199 (1982).

68. T. E. Gureyev, A. Roberts, and K. A. Nugent, “Phase retrieval with the transport-of-intensity equation: matrix solution with use of Zernike polynomials,” *J. Opt. Soc. Am. A* **12**, 1932 (1995).

69. G. Yang, B. Dong, B. Gu, J. Zhuang, and O. K. Ersoy, “Gerchberg-Saxton and Yang-Gu algorithms for phase retrieval in a nonunitary transform system: a comparison,” *Appl. Opt.* **33**, 209–218 (1994).

70. J. R. Fienup and A. M. Kowalczyk, “Phase retrieval for a complex-valued object by using a low-resolution image,” *J. Opt. Soc. Am. A* **7**, 450 (1990).

71. J. R. Fienup, “Lensless coherent imaging by phase retrieval with an illumination pattern constraint,” *Opt. Express* **14**, 498–508 (2006).

72. D. L. Misell, “An examination of an iterative method for the solution of the phase problem in optics and electron optics: I. Test calculations,” *J. Phys. D. Appl. Phys.* **6**, 2200–2216 (1973).

73. G. R. Brady, M. Guizar-Sicairos, and J. R. Fienup, “Optical wavefront measurement using phase retrieval with transverse translation diversity,” *Opt. Express* **17**, 624 (2009).

74. J. M. Rodenburg and H. M. L. Faulkner, “A phase retrieval algorithm for shifting illumination,” *Appl. Phys. Lett.* **85**, 4795 (2004).

75. G. Pedrini, W. Osten, and Y. Zhang, “Wave-front reconstruction from a sequence of interferograms recorded at different planes,” *Opt. Lett.* **30**, 833 (2005).

76. A. Anand, V. K. Chhaniwal, P. F. Almoro, G. Pedrini, and W. Osten, “Shape and deformation measurements of 3D objects using volume speckle field and phase retrieval,” *Opt. Lett.* **34**, 1522–1524 (2009).

77. P. F. Almoro, G. Pedrini, A. Anand, W. Osten, and S. G. Hanson, “Angular displacement and deformation analyses using a speckle-based wavefront sensor,” *Appl. Opt.* **48**, 932–940 (2009).

78. K. A. Nugent, “X-ray noninterferometric phase imaging: a unified picture,” *J. Opt. Soc. Am. A* **24**, 536 (2007).

79. P. F. Almoro, G. Pedrini, and W. Osten, “Complete wavefront reconstruction using sequential intensity measurements of a volume speckle field,” *Appl. Opt.* **45**, 8596–8605 (2006).

80. P. F. Almoro, A. M. S. Maallo, and S. G. Hanson, “Fast-convergent algorithm for speckle-based phase retrieval and a design for dynamic wavefront sensing,” *Appl. Opt.* **48**, 1485–1493 (2009).

81. L. Camacho, V. Micó, Z. Zalevsky, and J. García, “Quantitative phase microscopy using defocusing by means of a spatial light modulator,” *Opt. Express* **18**, 6755–6766 (2010).

82. M. Agour, P. F. Almoro, and C. Falldorf, “Investigation of smooth wave fronts using SLM-based phase retrieval and a phase diffuser,” *J. Eur. Opt. Soc. Rapid Publ.* **7**, 12046 (2012).

83. P. F. Almoro, J. Glückstad, and S. G. Hanson, “Single-plane multiple speckle pattern phase retrieval using a deformable mirror.,” *Opt. Express*

18, 19304–19313 (2010).

84. A. Anand, G. Pedrini, W. Osten, and P. F. Almoro, "Wavefront sensing with random amplitude mask and phase retrieval," *Opt. Lett.* **32**, 1584–1586 (2007).

85. P. F. Almoro and S. G. Hanson, "Random phase plate for wavefront sensing via phase retrieval and a volume speckle field," *Appl. Opt.* **47**, 2979–2987 (2008).

86. J. L. Crowley and A. C. Sanderson, "Multiple resolution representation and probabilistic matching of 2-d gray-scale shape.," *IEEE Trans. Pattern Anal. Mach. Intell.* **9**, 113–121 (1987).

87. T. Lindeberg, "Scale-space for discrete signals," *IEEE Trans. Pattern Anal. Mach. Intell.* **12**, 234–254 (1990).

88. B. E. A. Saleh and M. C. Teich, *Fundamentals of photonics*, Second (John Wiley & Sons, Inc., Hoboken, 2007).

89. T. Acharya and P. Tsai, "Computational foundations of image interpolation algorithms," *Ubiquity ACM* **8** (2007).

90. D. Fraser, "Interpolation by the FFT revisited-an experimental investigation," *IEEE Trans. Acoust.* **37**, 665–675 (1989).

91. T. Smit, M. R. Smith and S. T. Nichols, "Efficient sinc function interpolation technique for center padded data," *IEEE Trans. Acoust.* **38**, 1512–1517 (1990).

92. L. P. Yaroslavsky, "Efficient algorithm for discrete sinc interpolation," *Appl. Opt.* **36**, 460–463 (1997).

93. A. M. Maiden, J. M. Rodenburg, and M. J. Humphry, "Optical ptychography: a practical implementation with useful resolution.," *Opt. Lett.* **35**, 2585–2587 (2010).

94. K. Matsushima and T. Shimobaba, "Band-limited angular spectrum method for numerical simulation of free-space propagation in far and near fields," *Opt. Express* **17**, 19662–19673 (2009).

95. N. Chen, J.-H. Park, and N. Kim, "Parameter analysis of integral Fourier hologram and its resolution enhancement," *Opt. Express* **7618**, L.-C. Chien, Ed., 761809–761809–8 (OSA, 2010).

96. J.-H. Park, J. Kim, and B. Lee, "Three-dimensional optical correlator using a sub-image array," *Opt. Express* **13**, 5116–5126 (2005).

97. J.-H. Park, S. Jung, H. Choi, Y. Kim, and B. Lee, "Depth extraction by use of a rectangular lens array and one-dimensional elemental image modification," *Appl. Opt.* **43**, 4882–4895 (2004).

98. M.-S. Kim, G. Baasantseren, N. Kim, and J.-H. Park, "Hologram generation of 3D objects using multiple orthographic view images," *J. Opt. Soc. Korea* **12**, 269–274 (2008).

99. M.-S. Kim, G. Baasantseren, N. Kim, J. Park, M.-Y. Shin, and K.-H. Yoo, "Fourier hologram generation of 3D objects using multiple orthographic view images captured by lens array," in *SPIE* **12**, H. I. Bjelkhagen and R. K. Kostuk, Eds., (2009).

100. J. W. Goodman, *Introduction to Fourier Optics-Problem Solutions*, 3rd ed. (Roberts & Co Publishers, Greenwood Village, 2005).

101. S. Kishk and B. Javidi, "Improved resolution 3D object sensing and recognition using time multiplexed computational integral imaging," *Opt. Express* **11**, 3528–3541 (2003).

102. J. Hong, Y. Kim, H.-J. Choi, J. Hahn, J. Park, H. Kim, S. Min, N. Chen, and B. Lee, "Three-dimensional display technologies of recent interest: principles, status, and issues," *Appl. Opt.* **50**, H87–115 (OSA, 2011).

103. J. Hong, J. Park, S. Jung, and B. Lee, "Depth-enhanced integral

imaging by use of optical path control," *Opt. Lett.* **29**, 1790–1792 (2004).

104. J. Jang and B. Javidi, "Improved viewing resolution of three-dimensional integral imaging by use of nonstationary micro-optics," *Opt. Lett.* **27**, 324–326 (2002).

105. L. Erdmann and K. J. Gabriel, "High-resolution digital integral photography by use of a scanning microlens array," *Appl. Opt.* **40**, 5592–5599 (2001).

106. Y.-T. Lim, J.-H. Park, K.-C. Kwon, and N. Kim, "Resolution-enhanced integral imaging microscopy that uses lens array shifting," *Opt. Express* **17**, 19253–19263 (2009).

107. B. Lee, S. Jung, S.-W. Min, and J.-H. Park, "Three-dimensional display by use of integral photography with dynamically variable image planes," *Opt. Lett.* **26**, 1481–1482 (2001).

108. J. Park, K. Hong, and B. Lee, "Recent progress in three-dimensional information processing based on integral imaging," *Appl. Opt.* **48**, H77–94 (2009).

109. L. Middleton and J. Sivaswamy, *Hexagonal Image Processing: A Practical Approach* (Springer, 2006).

110. G. Jurasinski and C. Beierkuhnlein, "Spatial patterns of biodiversity–assessing vegetation using hexagonal grids," *Biol. Environ. ...* **106B**, 401–411 (2006).

111. D. P. I. Etersent, D. Petersen, and D. Middleton, "Sampling and reconstruction of wave-number-limited functions in N-dimensional euclidean spaces," *Inf. Control* **323** (1962).

112. P. K. Murphy and N. C. Gallagher, "Hexagonal sampling techniques applied to Fourier and Fresnel digital holograms," *J. Opt. Soc. Am.* **72**, 929 (1982).

113. S. Baronti, A. Capanni, A. Romoli, L. Santurri, and R. Vitulli, “On detector shape in hexagonal sampling grids,” in *SPIE* **4540**, H. Fujisada, J. B. Lurie and K. Weber, Eds.. (2001).

114. J.-H. Park, D. Han, and N. Kim, “Capture of the three-dimensional information based on integral imaging and its sampling analysis,” in *SPIE* **7848**, Y. Sheng, C. Yu and L. Chen, Eds.. (2010).

115. N. Chen, J. Yeom, J.-H. Park, and B. Lee, “High-resolution Fourier hologram generation using hexagonal lens array based on integral imaging,” *Dig. Int. Meet. Inf. Conf.*, 5–6 (2011).

116. A. Vincent, “Adaptive reconstruction of intermediate views from stereoscopic images,” *IEEE Trans. Circuits Syst. Video Technol.* **16**, 102–113 (2006).

117. J.-H. Park, G. Baasantseren, N. Kim, G. Park, J.-M. Kang, and B. Lee, “View image generation in perspective and orthographic projection geometry based on integral imaging.,” *Opt. Express* **16**, 8800–8813 (2008).

118. N. T. Shaked, B. Katz, and J. Rosen, “Review of three-dimensional holographic imaging by multiple-viewpoint-projection based methods,” *Appl. Opt.* **48**, H120–36 (2009).

119. N. Chen, J. Yeom, J. Jung, J.-H. Park, and B. Lee, “Resolution comparison between integral-imaging-based hologram synthesis methods using rectangular and hexagonal lens arrays,” *Opt. Express* **19**, 26917–26927 (OSA, 2011).

120. M. Levoy, Z. Zhang, I. McDowall, and M. View, “Recording and controlling the 4D light field in a microscope using microlens arrays.,” *J. Microsc.* **235**, 144–162 (2009).

121. A. Orth and K. B. Crozier, “Light field moment imaging,” *Opt. Lett.* **38**,

2666–2668 (2013).

122. R. Ng, “Fourier slice photography,” in *ACM SIGGRAPH 2005 Pap. - SIGGRAPH ’05*, (ACM Press, New York, New York, USA, 2005).

123. A. Veeraraghavan, R. Raskar, A. Agrawal, A. Mohan, and J. Tumblin, “Dappled photography: mask enhanced cameras for heterodyned light fields and coded aperture refocusing,” *ACM SIGGRAPH 2007 Pap. - SIGGRAPH ’07* **26**, 69 (ACM Press, New York, New York, USA, 2007).

124. C. Zuo, Q. Chen, and A. Asundi, “Light field moment imaging: comment,” *Opt. Lett.* **39**, 654 (2014).

125. A. Stern and B. Javidi, “Improved-resolution digital holography using the generalized sampling theorem for locally band-limited fields,” *J. Opt. Soc. Am. A. Opt. Image Sci. Vis.* **23**, 1227–1235 (2006).

126. A. Stern and B. Javidi, “Sampling in the light of Wigner distribution,” J. Opt. Soc. Am. A 21, 360 (2004).

초 록

실제 광학영상에서 획득하기 쉬운 세기성분뿐만 아니라 위상성분도 필요하다. 위상성분에는 물체의 모양, 깊이 등 중요한 정보들을 갖고 있다. 하지만 이는 일반 카메라로 획득하기에는 어려움들이 있음으로 특별한 기술들로 광파의 위상과 진폭을 기록하여야 한다. 그 방법들 중에서 회절 빔 세기를 반복적 측정방법 (iterative methods)과 홀로그래피 기술이 있다.

본 논문에서는 여러 개의 영상의 세기 값들만 이용하여 수렴하는 파면을 복원하는 방법을 제안하였다. 먼저 카메라로 획득한 세기영상을 서로 다른 해상도 레벨에 따라 재 샘플링하여 고해상도와 저 해상도 성분 영상으로 ss나눈다. 이 과정에 반복적 측정방법을 적용함으로 빠르게 수렴하는 위상 성분을 재생할 수 있다. 시뮬레이션과 실험으로부터, 제안된 방법은 기존의 방법들보다 위상복원 하는데 계산 속도가 50%이상 빠르다는 것을 확인 하였다.

일반 광원 아래에서 획득한 물체의 여러 시점영상들로부터 홀로그램을 생성하는 기법에 대하여, 홀로그램 재생영상의 해상도에 영향을 미치는 파라미터들을 분석하였다. 이 분석을 기반으로, 렌즈배열을 이용하여 홀로그램 재생 영상의 해상도를 향상시키는 방법을 제안 하였다. 홀로그램 생성에서 4각형 렌즈배열과 6각형 렌즈 배열을 사용하는 방법을 비교하였고, 그 결과 6각형 렌즈 배열을 사용하는 것이 샘플링을 더 효율적으로 할 수 있다는 것을 확인 하였다.

기존에 렌즈배열을 이용하여 수많은 시점영상들로부터 홀로그램을 생성 하는 방법에는 여러 가지 제약 조건들이 있음으로, 오직 서로 다른 깊이면 에서 촬영된 두 장의 영상만을 이용하여 홀로그램 생성 방법을 제안하였다. 제안된 방법은 기존 방법들에 존재했었던 샘플링 제약 요소들을 극복하였고 작은 물체로부터 큰 물체까지의 고해상도 홀로그램 영상을 재생 가능하다.

주요어: 홀로그래피, 파면 복원

학 번: 2010-31321